Pergamon

J. Mech. Phys. Solids, Vol. 42, No. 3, pp. 423–458, 1994

0022–5096/94 $6.00+0.00

FINITE ELEMENT SIMULATIONS OF SHEAR LOCALIZATION IN PLATE IMPACT

M. ZHOU, A. NEEDLEMAN and R. J. CLIFTON

Division of Engineering, Brown University, Providence, RI 02912, U.S.A.

(*Received* 3 *June* 1993; *in revised form* 18 *October* 1993)

ABSTRACT

SHEAR BAND development in a tungsten heavy alloy (WHA) during pressure–shear plate impact is analysed numerically. The alloy has a microstructure of hard tungsten grains embedded in a soft alloy matrix. A two-dimensional, plane strain model of the alloy microstructure is used in the computations. For this model microstructure a fully coupled thermo-mechanical initial boundary value problem is formulated and solved, accounting for finite deformations, inertia, heat conduction, thermal softening, strain hardening and strain-rate hardening. Calculations are carried out for distributions of uniform grains and for microstructures obtained from digitized micrographs of the actual alloy. The effects of variations in grain volume fraction and grain size are considered. Experiments and the numerical calculations show that the two-phase alloy is more susceptible to shear banding than either of the constituent phases. While the onset of shear localization depends on the grain distribution and volume fraction, the shear band width is found to be set by heat conduction and is insensitive to the grain volume fraction and the grain morphology. The shear band width obtained from the calculations is in good agreement with what is observed in the experiments. Furthermore, the computed shapes of the deformed tungsten grains inside the band resemble closely the observed shapes of the deformed grains in the experiments.

1. INTRODUCTION

THE NEED TO UNDERSTAND dynamic plastic flow is of critical importance in a wide range of applications including high speed machining, high rate forming, explosive welding, armor penetration and crash-worthiness of vehicles. At high rates of straining, the thermal softening that occurs because of the heating due to plastic dissipation, together with the lack of time for heat conduction, provides the main driving force for localization. Other physical mechanisms which are not specifically related to high strain rates, such as the yield vertex structure implied by the discreteness of crystallographic slip systems and progressive microrupture, may play significant roles in particular applications, see e.g. NEEDLEMAN and TVERGAARD (1992).

The pressure–shear plate impact experiment described by CLIFTON and KLOPP (1985) is an attractive configuration for studying dynamic plastic flow at shear strain rates of 10^5–$10^6\ s^{-1}$. In this experiment, sustained strain rates in excess of $10^5\ s^{-1}$ are achieved by sandwiching a thin foil specimen between two hard elastic plates (Fig. 1). Before unloading waves arrive from lateral boundaries, the stress and deformation states are characterized by plane wave conditions and large strains can be reached because the high pressure inhibits failure.

Shear band formation in a tungsten–nickel–iron (W–Ni–Fe) alloy was studied

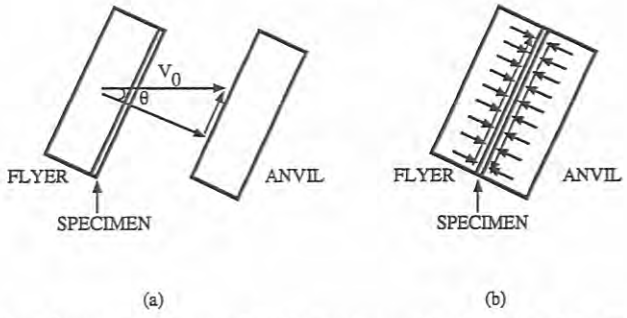

FIG. 1. Pressure–shear impact experiment of a thin specimen; (a) schematic of the pressure–shear plate impact configuration; (b) sandwich configuration of the experiment.

experimentally by ZHOU *et al.* (1992), using pressure–shear impact. The alloy consists of hard, more or less spherical, tungsten grains in a soft nickel–iron–tungsten matrix. Shear banding is especially important in this alloy because its performance as a long rod projectile for penetrating heavy armor appears to depend on the stability of its plastic flow at high strain rates. In the pressure–shear impact experiments, shear bands form at nominal shear strains of the order of 1–1.5 and are 5–10 μm wide. The intense shearing involves the hard tungsten grains as well as the soft matrix. ZHOU *et al.* (1992) also reported results of a finite element calculation for an idealized microstructure. The computed shear band morphology is remarkably similar to that observed in samples recovered from the impact experiments.

There is an extensive literature on the one-dimensional problem of thermal softening induced localization in simple shear (RECHT, 1964; CLIFTON, 1980; WRIGHT and WALTER, 1987; BAI, 1981, 1982; MERZER, 1982; MOLINARI and CLIFTON, 1987; DUFFY and CHI, 1992; BATRA and KIM, 1992; SHAWKI and CLIFTON, 1989). Such formulations do not, however, consider the microstructural interactions that can dominate the evolution of localized deformation in composite microstructures, such as that of the WHA alloy considered here.

In the present paper, a series of finite element calculations are carried out to model the experiments of ZHOU *et al.* (1992). The material is modelled as a composite consisting of two phases, i.e. the hard tungsten grains and soft matrix. The coupled thermal–mechanical problem is formulated as in LEMONDS and NEEDLEMAN (1986), but with full account of material inertia. Strain hardening, strain rate sensitivity, thermal softening and heat conduction are incorporated into the computational model. The analyses are carried out using a plane strain formulation; consequently the tungsten grains are modelled as cylinders rather than as spheres. The boundary and initial conditions here are consistent with a state of simple shear. Thermo-viscoplastic stress–strain relations for the tungsten grains and for the matrix are obtained by fitting the results of independent experiments.

Comparisons are made between the results obtained from pressure–shear impact experiments on the alloy and predictions from numerical calculations using digitized microstructures of the actual alloy. Good agreement is found for the shear band morphologies, shear band width and the stress–strain relations. Based on this agree-

ment, computer simulations are then carried out to explore the effects of such microstructural aspects as grain volume fraction, grain size and grain size distribution on localization—corresponding experimental parameter studies would be difficult to conduct.

Computer simulation is also used to identify the factor that sets the shear band width in the experiments of ZHOU *et al.* (1992). Several length scales, e.g. the characteristic length associated with heat conduction and the grain size are candidates for determining the shear band width. The results obtained here indicate that the length scale associated with heat conduction determines the shear band width in the circumstances considered.

2. MATERIAL BEHAVIOR

The tungsten–nickel–iron alloy studied by ZHOU *et al.* (1992) contains 93% W, 4.9% Ni and 2.1% Fe by weight. Figure 2(a) shows the microstructure of this material, which is typical of such alloys, consisting of nearly spherical grains of tungsten embedded in a soft matrix. The deformed microstructure of a thin foil of WHA after a pressure–shear plate impact experiment is shown in Fig. 2(b). The initial thickness of the specimen is 87 μm. The micrograph shows deep etching of the grains so that the structure of the deformed matrix and grains are clearly revealed. A band of intense shear deformation, which involves both the tungsten grains and the matrix, is formed in the middle of the thin foil. The width of the band is 5–10 μm. Note the tear-drop shape of the grains near the middle of the band. The specimen is slightly bent in the micrograph. This occurred after the experiment when the specimen was arrested inside a catcher filled with soft lead plates.

Characterization of the individual phases as well as of the composite tungsten heavy alloy (WHA) is based on data from pressure–shear plate impact, torsional Kolsky bar and quasi-static torsion experiments by ZHOU *et al.* (1992) and ZHOU (1993) to determine the response over a wide range of strain rate, from 10^{-4} to $7 \times 10^{5}\ s^{-1}$. For these experiments, the tungsten, the matrix and the WHA were all cross-rolled to a thickness reduction of 8% in each direction to obtain comparable dislocation structures so that direct comparisons could be made between the response of the WHA and its constituents. Figure 3(a) shows the rate sensitivities of the alloy matrix, the tungsten grains and the composite tungsten heavy alloy. Due to the brittle nature of pure tungsten and the lack of pressure in the quasi-static torsion and torsional Kolsky bar experimental configurations, rate sensitivity parameters cannot be obtained for tungsten grains for strain rates under $10^{4}\ s^{-1}$. The tungsten grains are assumed to have the same strain rate sensitivity at low strain rates, as that measured for WHA in quasi-static torsion and torsional Kolsky bar experiments. The matrix exhibits lower strain rate sensitivity than the grains and the composite tungsten heavy alloy at high strain rates. Figure 3(b) shows the thermal softening behavior of the constituent phases and the overall alloy. Results reported by ANDREWS *et al.* (1992) on the flow stress at strain rates of the order of $10^{3}\ s^{-1}$, BOSE *et al.* (1988) and O'DONNELL and WOODWARD (1990) on the temperature dependence of the flow stress for similar tungsten heavy alloys are also shown in Fig. 3. To characterize the thermal softening

behavior, it is assumed that the stress-carrying capacity of each material vanishes when the temperature reaches the corresponding melting point. Partly because of their different melting temperatures, pure tungsten and the matrix have very different thermal softening rates. The softening behavior for WHA is also shown for illustrative purposes. In the analyses presented in this paper, a characterization of the mechanical response of WHA is not required because the response of each phase is used in the simulations.

3. Analytical Formulation

3.1. *Momentum balance*

A convected coordinate, Lagrangian formulation of the field equations is used as, for example, in LeMonds and Needleman (1986), Needleman (1989), and Needleman and Tvergaard (1991). The independent variables are the particle coordinates ξ^i in the initial stress free configuration and time, t. A material point intially at $\mathbf{x}$ assumes a position $\bar{\mathbf{x}}$ in the current configuration. The displacement vector $\mathbf{u}$ and the deformation gradient tensor are defined by

$$\mathbf{u} = \bar{\mathbf{x}} - \mathbf{x}, \quad \mathbf{F} = \frac{\partial \bar{\mathbf{x}}}{\partial \mathbf{x}}. \tag{3.1}$$

In component form, the dynamic principle of virtual work is

$$\int_V \tau^{ij} \delta E_{ij} \, \mathrm{d}V = \int_S f^i \delta u_i \, \mathrm{d}S - \int_V \rho \frac{\partial^2 u^i}{\partial t^2} \delta u_i \, \mathrm{d}V, \tag{3.2}$$

where V, S and ρ are the volume, surface and mass density, respectively, of the body in the reference configuration, and τ^{ij} are the contravariant components of Kirchhoff stress ($\boldsymbol{\tau} = J\boldsymbol{\sigma} = \det|\mathbf{F}|\boldsymbol{\sigma}$, with $\boldsymbol{\sigma}$ the Cauchy stress tensor) on the deformed convected coordinate net. Also,

$$f^i = (\tau^{ij} + \tau^{kj} u^i_{,k}) n_j, \tag{3.3}$$

are the tractions on a surface with normal $\mathbf{n}$ in the reference configuration and

$$E_{ij} = \tfrac{1}{2}(u_{i,j} + u_{j,i} + u^k_{,i} u_{k,j}), \tag{3.4}$$

where $(\,)_{,i}$ denotes covariant differentiation in the reference frame.

3.2. *Constitutive relation*

For elastic–plastic flow, the basic kinematic assumption is (Lee, 1969)

$$\mathbf{F} = \mathbf{F}^{\mathrm{e}} \cdot \mathbf{F}^{\mathrm{p}}, \tag{3.5}$$

where $\mathbf{F}^{\mathrm{e}}$ represents the deformation gradient associated with thermo-elastic deformation and rigid body rotation, and $\mathbf{F}^{\mathrm{p}}$ is the deformation gradient associated with plastic flow only.

The rate of deformation, $\mathbf{D}$, and the spin, $\boldsymbol{\Omega}$, are the symmetric and anti-symmetric

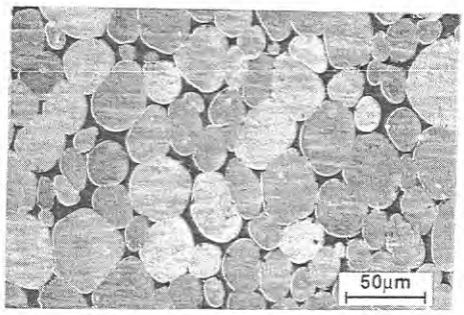

(a)

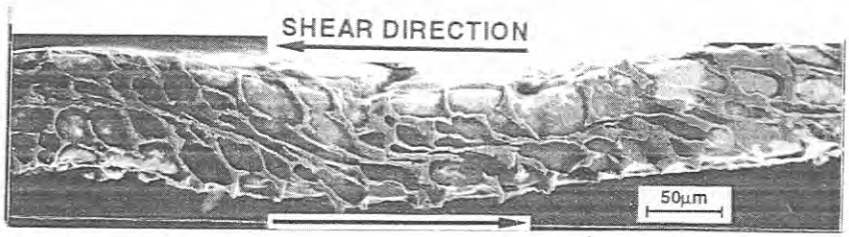

(b)

FIG. 2. (a) Microstructure of the tungsten heavy alloy before test; (b) deformed microstructure of the same alloy after pressure–shear plate impact test showing a shear band at the center.

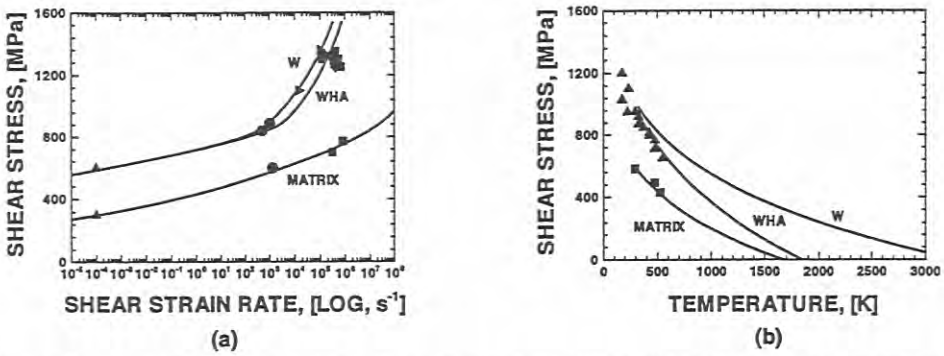

FIG. 3. Response of the constituent phases and the overall alloy; (a) rate sensitivities; (b) temperature dependence of the stress.

parts of $\dot{\mathbf{F}} \cdot \mathbf{F}^{-1}$,

$$\mathbf{D}+\boldsymbol{\Omega} = \dot{\mathbf{F}} \cdot \mathbf{F}^{-1} = \dot{\mathbf{F}}^{e} \cdot \mathbf{F}^{e-1} + \mathbf{F}^{e} \cdot \dot{\mathbf{F}}^{p} \cdot \mathbf{F}^{p-1} \cdot \mathbf{F}^{e-1}, \tag{3.6}$$

where $(\dot{\ })$ denotes $\partial(\ )/\partial t$ and $(\ )^{-1}$ denotes tensor inverse. The elastic and plastic parts of $\mathbf{D}$ and $\boldsymbol{\Omega}$ are given by

$$\mathbf{D}^{e}+\boldsymbol{\Omega}^{e} = \dot{\mathbf{F}}^{e} \cdot \mathbf{F}^{e-1}, \tag{3.7}$$

$$\mathbf{D}^{p}+\boldsymbol{\Omega}^{p} = \mathbf{F}^{e} \cdot \dot{\mathbf{F}}^{p} \cdot \mathbf{F}^{p-1} \cdot \mathbf{F}^{e-1}. \tag{3.8}$$

Attention is restricted to small elastic strains so that $\mathbf{F}^{e} = \mathbf{Q} \cdot (\mathbf{I}+\varepsilon)$, where $\mathbf{Q}$ is a rotation matrix which satisfies $\mathbf{Q}^{-1} = \mathbf{Q}^{T}$, $\mathbf{I}$ is the second order identity tensor and $\varepsilon = \varepsilon^{T}$, with $\|e\| \ll 1$. Only isotropic hardening solids for which $\boldsymbol{\Omega}^{p} = 0$ are considered. Furthermore, thermo-elastic coupling is assumed negligible and any temperature dependence of the elastic moduli is ignored. Under these conditions (POVIRK *et al.*, 1993),

$$\hat{\tau} = \dot{\tau} - \boldsymbol{\Omega} \cdot \tau + \tau \cdot \boldsymbol{\Omega} = \mathbf{L} : [\mathbf{D} - \mathbf{D}^{p} - \boldsymbol{\alpha}\dot{T}], \tag{3.9}$$

where $\hat{\tau}$ is the Jauman rate of Kirchhoff stress, $\mathbf{L}$ is the tensor of elastic moduli, $\boldsymbol{\alpha}$ is the thermal expansion tensor, T is the temperature and the dyadic product $\mathbf{A}:\mathbf{B}$ is $A^{ij}\mathbf{B}_{ji}$. For isotropic thermo-elastic response,

$$\mathbf{L} = \frac{E}{1+\nu}\left[\mathbf{I}' + \frac{\nu}{1-2\nu}\mathbf{I} \otimes \mathbf{I}\right], \quad \boldsymbol{\alpha} = \alpha\mathbf{I}. \tag{3.10}$$

Here, $\mathbf{I}'$ is the fourth order identity tensor, E is Young's modulus, ν is Poisson's ratio, α is the thermal expansion coefficient and $\mathbf{A} \otimes \mathbf{B}$ denotes the tensor product.

For an isotropically hardening, viscoplastic solid $\mathbf{D}^{p}$ is given by

$$\mathbf{D}^{p} = \frac{3\dot{\bar{\varepsilon}}}{2\bar{\sigma}}\tau', \tag{3.11}$$

with $\dot{\bar{\varepsilon}}$ being the equivalent plastic strain rate and

$$\boldsymbol{\tau}' = \boldsymbol{\tau} - \tfrac{1}{3}(\boldsymbol{\tau} : \mathbf{I})\mathbf{I}, \quad \bar{\sigma}^2 = \tfrac{3}{2}\boldsymbol{\tau}' : \boldsymbol{\tau}'. \tag{3.12}$$

The viscoplastic response of each of the constituent materials is obtained experimentally (ZHOU *et al.*, 1992) for the strain-rate range of 10^{-4}–7×10^5 s^{-1} and is characterized by the following equations

$$\left.\begin{aligned} \dot{\bar{\varepsilon}} &= \frac{\dot{\varepsilon}_1 \dot{\varepsilon}_2}{\dot{\varepsilon}_1 + \dot{\varepsilon}_2}, \\ \dot{\varepsilon}_1 &= \dot{\varepsilon}_0 \left[\frac{\bar{\sigma}}{g(\bar{\varepsilon}, T)}\right]^m, \\ \dot{\varepsilon}_2 &= \dot{\varepsilon}_m \exp\left[-\frac{ag(\bar{\varepsilon}, T)}{\bar{\sigma}}\right], \\ g(\bar{\varepsilon}, T) &= \sigma_0 (1 + \bar{\varepsilon}/\varepsilon_0)^N \{1 - \beta[(T/T_0)^\kappa - 1]\}, \end{aligned}\right\} \tag{3.13}$$

where $\bar{\varepsilon} = \int_0^t \dot{\bar{\varepsilon}}\, \mathrm{d}t$ is the equivalent plastic strain; $\dot{\varepsilon}_0$ is a reference strain rate; m and a are rate sensitivity parameters, respectively, for strain rates below 10^3 s^{-1} and above 5×10^4 s^{-1}, σ_0 is a reference stress, ε_0 is a reference strain, N is the strain hardening exponent, T_0 is a reference temperature, and β and κ are thermal softening parameters. The function $g(\bar{\varepsilon}, T)$ represents the stress–strain relation at a quasi-static strain rate of $\dot{\varepsilon}_0$ and at temperature T. At $T = T_0$, $g(\bar{\varepsilon}, T) = \sigma_0(1 + \bar{\varepsilon}/\varepsilon_0)^N$.

The form (3.13) provides a smooth transition between the measured response $\dot{\bar{\varepsilon}} = \dot{\varepsilon}_1(\bar{\sigma}, \bar{\varepsilon})$ at strain rates less than 10^3 s^{-1}, and the limiting behavior $\dot{\bar{\varepsilon}} = \dot{\varepsilon}_2(\bar{\sigma}, \bar{\varepsilon})$ at strain rates greater than, say, 5×10^4 s^{-1}. The model (3.13) includes a limiting strain rate $\dot{\varepsilon}_m$ which is not available from experiments; a value 8×10^8 s^{-1} or greater is chosen, primarily for the numerical purpose of avoiding the need for unreasonably small time steps at early times when the shear stresses are large. These stresses are relaxed in a few nanoseconds. The uncertainty in the response of the material at small strains and at shear strain rates greater than, say, 10^7 s^{-1} is unavoidable at the present because of the lack of experimental data in this regime. This uncertainty may have an effect on the calculated initial impact response. However, this uncertainty in the initial response of the material is not expected to play a significant role in the shear band formation which occurs much later. The dependence of the normalized stress $\bar{\sigma}/g$ on the strain rate $\dot{\bar{\varepsilon}}$ characterized by (3.13) is shown schematically in Fig. 4.

3.3. *Energy balance and heat conduction*

The formulation of the energy balance and of the equation of heat conduction follows POVIRK *et al.* (1993), except for the inclusion of the kinetic energy term here. The balance of energy is expressed in terms of integrals over the reference configuration as

$$\int_V \rho \dot{e}\, \mathrm{d}V + \frac{\mathrm{d}}{\mathrm{d}t} \int_V \tfrac{1}{2}\rho \dot{\mathbf{u}} \cdot \dot{\mathbf{u}}\, \mathrm{d}V = \int_S \mathbf{f} \cdot \dot{\mathbf{u}}\, \mathrm{d}S - \int_S J\mathbf{n} \cdot \mathbf{F}^{-1} \cdot \bar{\mathbf{q}}\, \mathrm{d}S, \tag{3.14}$$

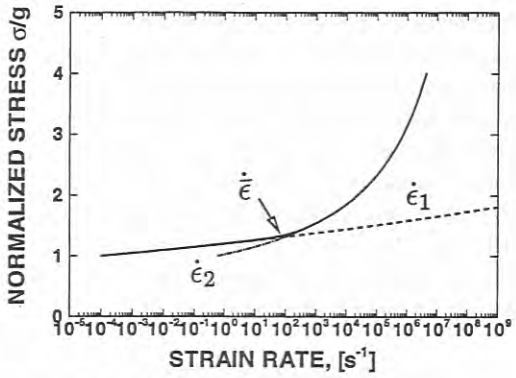

FIG. 4. Rate sensitivity formulation.

where e is the specific internal energy, $J = \det|\mathbf{F}|$ and $\bar{\mathbf{q}}$ is the heat flux across a surface element in the *current* configuration. Plastic straining is isochoric and, since the elastic strains remain small, $J = \det|\mathbf{F}^e| \approx 1$ (hence $\tau \approx \sigma$).

From

$$\int_S \mathbf{f}\cdot\mathbf{u}\,\mathrm{d}S = \int_V \tau:\mathbf{D}\,\mathrm{d}V + \frac{\mathrm{d}}{\mathrm{d}t}\int_V \tfrac{1}{2}\rho\dot{\mathbf{u}}\cdot\dot{\mathbf{u}}\,\mathrm{d}V, \tag{3.15}$$

one can rewrite (3.14) as

$$\int_V \rho\dot{e}\,\mathrm{d}V = \int_V \tau:\mathbf{D}\,\mathrm{d}V - \int_S J\mathbf{n}\cdot\mathbf{F}^{-1}\cdot\bar{\mathbf{q}}\,\mathrm{d}S. \tag{3.16}$$

Neglecting thermo-elastic coupling terms, using $J \approx 1$ and assuming that the heat capacity at constant stress can be approximated by the specific heat at constant pressure, one can reduce (3.16) to (POVIRK *et al.*, 1993)

$$\int_V \rho c_p \dot{T}\,\mathrm{d}V = \int_V \chi\tau:\mathbf{D}^p\,\mathrm{d}V - \int_V \frac{\partial}{\partial\mathbf{x}}\cdot\mathbf{F}^{-1}\cdot\bar{\mathbf{q}}\,\mathrm{d}V, \tag{3.17}$$

where c_p is the specific heat at constant pressure and χ is the portion of plastic work converted to heat; χ is taken to have the value 0.90, which is typical for metals (TAYLOR and QUINNEY, 1934).

The constitutive relation for the heat flux is specified as a linear relation between the heat flux vector and the temperature gradient. This relation is required to be independent of any superposed rigid body rotation, which precludes a general linear relation between $\bar{\mathbf{q}}$ and the temperature gradient in the current configuration, $\partial T/\partial\bar{\mathbf{x}}$. However, for isotropic solids we can write

$$\bar{\mathbf{q}} = -k\frac{\partial T}{\partial\bar{\mathbf{x}}}, \tag{3.18}$$

where k is the thermal conductivity. The relation (3.18) can be regarded as an

approximation to a more general relation in the intermediate, plastically deformed configuration for the special case of small elastic deformations and isotropic thermal conductivity. LEMONDS and NEEDLEMAN (1986) used a constitutive relation for isotropic heat conduction of the form $\mathbf{q} = k\,\partial T/\partial \mathbf{x}$, with $\mathbf{q}$ being the heat flux across the surface in the reference configuration. While satisfying the necessary invariance requirements, this leads to a dependence of the apparent conductivity on prior plastic flow at large plastic strains, which is not in accord with the expected behavior. However, some calculations here were carried out through the onset of shear band development using the heat conduction constitutive relation of LEMONDS and NEEDLEMAN (1986) instead of (3.18), and the difference between the two sets of results was negligible.

The variational equation obtained from (3.17), and used in the finite element formulation is

$$\int_V \rho c_p \dot{T}\delta T\,\mathrm{d}V = \int_V \chi\tau : \mathbf{D}^p \delta T\,\mathrm{d}V + \int_S k\left(\mathbf{F}^{-1}\cdot\mathbf{F}^{-T}\cdot\frac{\partial T}{\partial \mathbf{x}}\right)\cdot\mathbf{n}\delta T\,\mathrm{d}S - \int_V k(\mathbf{F}^{-1}\cdot\mathbf{F}^{-T}\cdot\frac{\partial T}{\partial \mathbf{x}})\cdot\frac{\partial \delta T}{\partial \mathbf{x}}\,\mathrm{d}V. \quad (3.19)$$

3.4. *Boundary and initial conditions*

A schematic of the sandwich configuration of the pressure-shear impact experiment is shown in Fig. 1, as described by CLIFTON and KLOPP (1985). The specimen, a thin foil 50–100 μm in thickness and bonded to the front of a flyer plate, impacts a stationary anvil plate. The flyer and anvil are made of the same material, which is chosen so that their response remains linear elastic throughout the experiment. The parallel impact faces are inclined relative to the direction of approach to achieve combined pressure–shear loading. All surfaces are lapped flat to approximately one-half the wavelength of sodium light (less than 0.3 μm surface height variation over the diameter). Nominal shear strain rates up to $7\times10^5\ \mathrm{s}^{-1}$ are obtained.

The experiment lasts approximately 2 μs following initial impact. During this period the flyer and anvil plates act effectively as infinite half-planes for the following reasons: (1) no waves initiated from the cylindrical periphery or reflected from the free ends arrive at the central part of the specimen–flyer and specimen–anvil interfaces, so that plane wave conditions apply; (2) temperature changes in the flyer and anvil plates are limited to within a small distance from the specimen–flyer and specimen–anvil interfaces and heat transfer is not affected by the end and cylindrical surfaces of the plates. Therefore, neither the mechanical process of dynamic deformation and wave propagation, nor the thermal process of heat generation and transfer is influenced by the finite lateral extent of the specimen. In Fig. 5 the impact face (the specimen–anvil interface) is located at $\xi^1 = h$ and the specimen–flyer interface is at $\xi^1 = 0$. The interval $0 \leqslant \xi^2 = l$ is identified with a representative interval in the central portion of the specimen; periodic boundary conditions are imposed at $\xi^2 = 0$ and $\xi^2 = l$.

The initial configuration is taken to be the configuration at which the specimen comes into contact with the anvil. At this instant $t = 0$ and the specimen is stress free

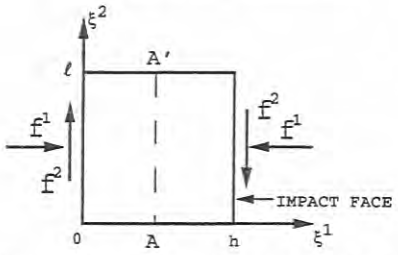

FIG. 5. Problem formulation. The impact face is at $\xi^1 = h$ and the flyer–specimen interface is at $\xi^1 = 0$. Periodic thermal and mechanical B.C.s are specified along $\xi^2 = 0$ and $\xi^2 = l$. The arrows show the actual directions of the traction components on the specimen during the experiment.

except at the impact face. Also, the specimen, the flyer and the anvil are at the uniform temperature T_0. However, the specimen and the flyer are undergoing a rigid body translation with velocity V_0 and at an angle θ with respect to the reference Cartesian frame. Thus, in the specimen

$$\left.\begin{aligned} \dot{u}^1(\xi^1, \xi^2, 0) &= V_0 \cos\theta, \\ \dot{u}^2(\xi^1, \xi^2, 0) &= V_0 \sin\theta, \end{aligned}\right\}; \quad \begin{aligned} &0 \leqslant \xi^1 < h, \\ &0 \leqslant \xi^2 \leqslant l. \end{aligned} \tag{3.20}$$

At $t = 0$ the instantaneous response on both sides of the specimen–anvil interface is elastic. Conservation of momentum together with continuity of velocities and tractions gives

$$\left.\begin{aligned} \dot{u}^1(h, \xi^2, 0) &= V_0 \cos\theta \frac{(\rho c_L)_s}{(\rho c_L)_s + (\rho c_L)_a}, \\ \dot{u}^2(h, \xi^2, 0) &= V_0 \sin\theta \frac{(\rho c_s)_s}{(\rho c_s)_s + (\rho c_s)_a}, \end{aligned}\right\}; \quad 0 \leqslant \xi^2 \leqslant l, \tag{3.21}$$

and the traction components f^i are given by

$$\left.\begin{aligned} f^1(h, \xi^2, 0) &= -V_0 \cos\theta \frac{(\rho c_L)_s (\rho c_L)_a}{(\rho c_L)_s + (\rho c_L)_a}, \\ f^2(h, \xi^2, 0) &= -V_0 \sin\theta \frac{(\rho c_s)_s (\rho c_s)_a}{(\rho c_s)_s + (\rho c_s)_a}, \end{aligned}\right\}; \quad 0 \leqslant \xi^2 \leqslant l, \tag{3.22}$$

where $(\,)_s$ and $(\,)_a$ denote quantities associated with the specimen and the anvil, respectively, and

$$c_L = \sqrt{\frac{E(1-\nu)}{(1+\nu)(1-2\nu)\rho}}, \quad c_s = \sqrt{\frac{E}{2(1+\nu)\rho}}. \tag{3.23}$$

Since attention is restricted to a time interval before any waves are reflected back to the flyer–specimen or anvil–specimen interfaces, and since the flyer and anvil each remain elastic, the impact boundary conditions for $t > 0$ are determined by the conservation and continuity conditions obtained from one-dimensional elastic wave propagation in the flyer and anvil. According to one-dimensional elastic wave theory

all states at the flyer–specimen interface must satisfy

$$\left.\begin{aligned} -f^1+(\rho c_L)_f \dot{u}^1 &= (\rho c_L)_f V_0 \cos\theta, \\ -f^2+(\rho c_s)_f \dot{u}^2 &= (\rho c_s)_f V_0 \sin\theta, \end{aligned}\right\}; \quad \xi^1 = 0, \tag{3.24}$$

where $(\ )_f$ denotes quantities associated with the flyer.

Similarly, all states at the specimen–anvil impact face must satisfy

$$\left.\begin{aligned} f^1+(\rho c_L)_a \dot{u}^1 &= 0, \\ f^2+(\rho c_s)_a \dot{u}^2 &= 0, \end{aligned}\right\}; \quad \xi^1 = h. \tag{3.25}$$

Because any temperature change is driven by plastic deformation in the specimen, the temperature remains uniform until plastic flow initiates. The thermal boundary conditions are then specified by requiring continuity of the heat flux across the specimen-flyer and the specimen–anvil interfaces. The flyer and the anvil are modelled as half-spaces with a prescribed boundary temperature history, which is obtained from the thermo-mechanical solution for the specimen. The temperature gradient at the interface with the specimen is then obtained from the solution of the heat equation. For the flyer, the half-space is $-\infty < \xi^1 \leqslant 0$, while for the anvil the half-space is $h \leqslant \xi^1 < \infty$. Since the flyer and anvil remain linear elastic during the experiment, $\mathbf{F}$ is approximately a rotation in the flyer and in the anvil, so that for one-dimensional heat conduction (3.17) yields

$$\dot{T} = \left(\frac{k}{\rho c_p}\right)_a T_{,11} = D_a^2 T_{,11} \quad h \leqslant \xi^1 < \infty, \quad t \geqslant 0; \tag{3.26}$$

$$T(h,t) = f(t), \quad t \geqslant 0; \tag{3.27}$$

$$T(\xi^1, 0) = T_0, \quad h \leqslant \xi^1 < \infty$$

for the anvil, where D_a^2 is the thermal diffusivity of the anvil. The solution to (3.26) with the initial and boundary conditions (3.27) is

$$T(\xi^1,t) = T_0 + \int_0^t [f(\tau)-T_0] \frac{\xi^1-h}{2D_a\sqrt{\pi(t-\tau)^3}} \exp\left[\frac{-(\xi^1-h)^2}{4D_a^2(t-\tau)}\right] d\tau, \tag{3.28}$$

$$T_{,1}(\xi^1,t) = \int_0^t \exp\left[\frac{-(\xi^1-h)^2}{4D_a^2(t-\tau)}\right] \frac{[f(\tau)-T_0]}{2D_a\sqrt{\pi(t-\tau)^3}} \left[1-\frac{(\xi^1-h)^2}{2D_a^2(t-\tau)}\right] d\tau, \tag{3.29}$$

for $t > 0$. A similar solution is obtained for the flyer.

The solution given in (3.28) and (3.29) can be evaluated for any time t for which the boundary temperature history $f(\tau)$, $0 \leqslant \tau < t$ is known. The integral functions defined on the right-hand sides of (3.28) and (3.29) have a discontinuity at $\xi^1 = h$. Consequently, the values of T and $T_{,1}$ at $\xi^1 = h$ are defined only in the limit

$$T(h,t) = \lim_{\xi^1 \to h^+} T(\xi^1,t) = f(t),$$

$$T_{,1}(h,t) = \lim_{\xi^1 \to h^+} \frac{\partial T(\xi^1,t)}{\partial \xi^1}.$$

In the numerical implementation, the limit is not evaluated explicitly. Instead, the value of $T_{,1}$ at $h+\Delta h$ is used to calculate the heat flux at the anvil–specimen and flyer–specimen interfaces, where $\Delta h/h$ is small. Specifically, in the calculations $\Delta h/h = 1/87$ (the specimen thickness is 87 μm and $T_{,1}$ is evaluated 1 μm inside the flyer and the anvil).

The periodic boundary conditions along $\xi^2 = 0$ and $\xi^2 = l$ (see Fig. 5) are simply

$$\mathbf{u}(\xi^1, 0, t) = \mathbf{u}(\xi^1, l, t), \tag{3.30}$$

$$T(\xi^1, 0, t) = T(\xi^1, l, t). \tag{3.31}$$

4. FINITE ELEMENT METHOD

The discretization is based on triangular elements arranged in "crossed triangle" quadrilaterals. Displacements and temperature are taken to vary linearly over the triangular elements. When the finite element approximations of the displacement and temperature fields are substituted into the momentum balance (3.2) and the energy balance (3.19), the resulting equations take the form,

$$\mathbf{M}\frac{\partial^2 \mathbf{U}}{\partial t^2} = \mathbf{R}, \tag{4.1}$$

and

$$\mathbf{C}\frac{\partial \mathbf{T}}{\partial t} = -\mathbf{K}\mathbf{T} + \mathbf{H}, \tag{4.2}$$

where $\mathbf{U}$ is the vector of nodal displacements, $\mathbf{T}$ is the vector of nodal temperatures, $\mathbf{M}$, $\mathbf{C}$ and $\mathbf{K}$ are, respectively, the mass, the heat capacitance and the heat conductance matrices, and $\mathbf{R}$ and $\mathbf{H}$ are the mechanical and thermal force vectors.

A lumped mass matrix is used in (4.1), for reasons of efficiency and accuracy (KRIEG and KEY, 1973). Additionally, a lumped heat capacitance matrix is used in (4.2). In order to verify the accuracy of the integration of (4.2) with a lumped capacitance matrix, numerical results for a purely thermal problem involving non-uniform heat sources distributed on a rectangular area were compared with an analytical solution and good agreement was found.

At time t_n, the state of the specimen (displacements, velocities, temperatures, internal variables, etc.) is presumed known. The displacements and velocities at $t_{n+1} = t_n + \Delta t_n$ are obtained by integrating the equations of motion using an explicit integration method, the Newmark β-method, with $\beta = 0$ and $\gamma = 0.5$ (BELYTSCHKO *et al.*, 1976).

$$\frac{\partial^2 \mathbf{U}^{n+1}}{\partial t^2} = \mathbf{M}^{-1}\mathbf{R}, \tag{4.3}$$

$$\frac{\partial \mathbf{U}^{n+1}}{\partial t} = \frac{\partial \mathbf{U}^n}{\partial t} + \tfrac{1}{2}\Delta t_n\left(\frac{\partial^2 \mathbf{U}^n}{\partial t^2} + \frac{\partial^2 \mathbf{U}^{n+1}}{\partial t^2}\right), \tag{4.4}$$

$$\mathbf{U}^{n+1} = \mathbf{U}^n + \Delta t_n \frac{\partial \mathbf{U}^n}{\partial t} + \tfrac{1}{2}(\Delta t_n)^2 \frac{\partial^2 \mathbf{U}^n}{\partial t^2}, \tag{4.5}$$

where $(\ )^{-1}$ denotes the matrix inverse.

At this point the plastic dissipation rate, $\boldsymbol{\tau} : \mathbf{D}^p$, is calculated and its contribution to the thermal force $\mathbf{H}^n$ determined. The temperatures at t_{n+1} are obtained via

$$\frac{\partial \mathbf{T}^{n+1}}{\partial t} = \mathbf{C}^{-1}(-\mathbf{K}^n \mathbf{T}^n + \mathbf{H}^n), \tag{4.6}$$

$$\mathbf{T}^{n+1} = \mathbf{T}^n + \Delta t_n \frac{\partial \mathbf{T}^{n+1}}{\partial t}. \tag{4.7}$$

The stress components are then updated by

$$\tau^{kl}_{t_n + \Delta t_n} = \tau^{kl}_{t_n} + \dot{\tau}^{kl} \Delta t_n. \tag{4.8}$$

The rate tangent modulus expansion of PEIRCE *et al.* (1984) is used to obtain $\dot{\tau}^{kl}$. The equivalent plastic strain rate is expressed as a linear combination of its values at t_n and t_{n+1},

$$\dot{\bar{\varepsilon}} = (1-\theta)\dot{\bar{\varepsilon}}_{t_n} + \theta \dot{\bar{\varepsilon}}_{t_n + \Delta t_n}, \quad 0 \leqslant \theta \leqslant 1, \tag{4.9}$$

with $\dot{\bar{\varepsilon}}_{t_n + \Delta t_n}$ approximated by a first order Taylor series expansion in $\bar{\sigma}$, $\bar{\varepsilon}$ and T,

$$\dot{\bar{\varepsilon}}_{t_n + \Delta t_n} = \dot{\bar{\varepsilon}}_{t_n} + \Delta t_n \left[\left. \frac{\partial \dot{\bar{\varepsilon}}}{\partial \bar{\sigma}} \right|_{t_n} \dot{\bar{\sigma}} + \left. \frac{\partial \dot{\bar{\varepsilon}}}{\partial \bar{\varepsilon}} \right|_{t_n} \dot{\bar{\varepsilon}} + \left. \frac{\partial \dot{\bar{\varepsilon}}}{\partial T} \right|_{t_n} \dot{T} \right]. \tag{4.10}$$

The plastic consistency condition, the stress-rate relation (3.9), (4.9) and (4.10) give

$$\dot{\bar{\varepsilon}} = \frac{\dot{\bar{\varepsilon}}_{t_n}}{1+\zeta} + \frac{\zeta}{(1+\zeta)H} \left[\left(\frac{3\tau'}{2\bar{\sigma}} \right) : \mathbf{L} : \mathbf{D} + \dot{T} \frac{\partial \dot{\bar{\varepsilon}} / \partial T}{\partial \dot{\bar{\varepsilon}} / \partial \bar{\sigma}} \right], \tag{4.11}$$

where

$$\left.\begin{aligned} \zeta &= \theta \Delta t_n \frac{\partial \dot{\bar{\varepsilon}}}{\partial \bar{\sigma}} H, \\ H &= \frac{3E}{2(1+\nu)} - \frac{\partial \dot{\bar{\varepsilon}} / \partial \bar{\varepsilon}}{\partial \dot{\bar{\varepsilon}} / \partial \bar{\sigma}}. \end{aligned}\right\} \tag{4.12}$$

From (3.13),

$$\frac{\partial \dot{\bar{\varepsilon}}}{\partial \bar{\sigma}} = \frac{\dot{\varepsilon}_1 \dot{\varepsilon}_2}{(\dot{\varepsilon}_1 + \dot{\varepsilon}_2)^2} \frac{1}{\bar{\sigma}} \left[\dot{\varepsilon}_1 \left(\frac{ag}{\bar{\sigma}} \right) + \dot{\varepsilon}_2 m \right], \tag{4.13}$$

$$\left.\begin{aligned} \frac{\partial \dot{\bar{\varepsilon}} / \partial T}{\partial \dot{\bar{\varepsilon}} / \partial \bar{\sigma}} &= -\left(\frac{\bar{\sigma}}{g} \right) \frac{\partial g}{\partial T}, \\ \frac{\partial \dot{\bar{\varepsilon}} / \partial \bar{\varepsilon}}{\partial \dot{\bar{\varepsilon}} / \partial \bar{\sigma}} &= -\left(\frac{\bar{\sigma}}{g} \right) \frac{\partial g}{\partial \bar{\varepsilon}}, \end{aligned}\right\} \tag{4.14}$$

and

$$\left.\begin{aligned}\frac{\partial g}{\partial T} &= \sigma_0(1+\bar{\varepsilon}/\varepsilon_0)^N\left\{-\beta_\kappa\left[(T/T_0)^{\kappa-1}\frac{1}{T_0}\right]\right\},\\ \frac{\partial g}{\partial \bar{\varepsilon}} &= \sigma_0 N(1+\bar{\varepsilon}/\varepsilon_0)^{N-1}\frac{1}{\varepsilon_0}\{1-\beta[(T/T_0)^\kappa-1]\}.\end{aligned}\right\} \tag{4.15}$$

The values of the temperature, T, and temperature rates, $\dot{T}$, at the finite element integration points (the triangle centroids) for use in (4.11)–(4.15) are obtained from the nodal values in (4.6) and (4.7). The plastic strain rate $\dot{\bar{\varepsilon}}$ in (4.11) together with (3.9)–(3.11) determines $\dot{\tau}^{kl}$ for use in (4.8). The plastic strain is updated using $\bar{\varepsilon}_{t_n+\Delta t_n} = \bar{\varepsilon}_{t_n} + \dot{\bar{\varepsilon}}\Delta t_n$, with $\dot{\bar{\varepsilon}}$ computed from (4.11). Then, $g(\bar{\varepsilon}, T)$ is calculated from the last of (3.13) and $\bar{\sigma}$ is determined from the consistency condition (3.12).

The periodic boundary conditions (3.30) and (3.31) are implemented by computing the nodal accelerations and temperature rates on $\xi^2 = 0$ and $\xi^2 = l$ as

$$\left.\frac{\partial^2 \mathbf{U}}{\partial t^2}\right|_A = \left.\frac{\partial^2 \mathbf{U}}{\partial t^2}\right|_{A'} = \frac{(\mathbf{R})_A + (\mathbf{R})_{A'}}{(\mathbf{M})_A + (\mathbf{M})_{A'}}, \tag{4.16}$$

and

$$\dot{\mathbf{T}}|_A = \dot{\mathbf{T}}|_{A'} = \frac{(-\mathbf{KT}+\mathbf{H})_A + (-\mathbf{KT}+\mathbf{H})_{A'}}{(\mathbf{C})_A + (\mathbf{C})_{A'}}, \tag{4.17}$$

where $(\,)_A$ and $(\,)_{A'}$ denote the components associated with the two nodes on $\xi^2 = 0$ and $\xi^2 = l$ that satisfy $(\xi^1)_A = (\xi^1)_{A'}$; $(\mathbf{M})_A$, $(\mathbf{M})_{A'}$, and $(\mathbf{C})_A$ and $(\mathbf{C})_{A'}$ are the corresponding nodal masses and nodal capacitances.

5. Numerical Results

The distribution of the constituent phases plays an important role in the response of the composite. The five grain–matrix distributions shown in Fig. 6 are analysed in the present investigation. In the calculations, a triangular element whose centroid falls inside a grain is assigned the tungsten material properties, otherwise it is given the material properties of the matrix. Distribution (a) consists of circular grains 39.2 μm in diameter; distribution (b) is distribution (a) rotated 90° counter-clockwise. When sheared along the directions shown in Fig. 6, these two distributions represent the two orientations in a closely packed array of circular grains that pose the least [Fig. 6(a)] and the most [Fig. 6(b)] resistance to shear deformation. Distribution (c) is a digitized microstructure of the actual alloy used in the experiments. Distribution (d) is the digitized microstructure with the grain size reduced by a factor of 1.75. Microstructures (a)–(d) have the same volume fraction of grains (87.7%). Figure 6(e) shows a distribution with a smaller grain volume fraction (76.8%), obtained from Fig. 6(d) by changing the material type of a uniform layer on the surface of each grain into that of the matrix. These grain–matrix distributions are used to investigate the effects of grain size, morphology and volume fraction on shear localization.

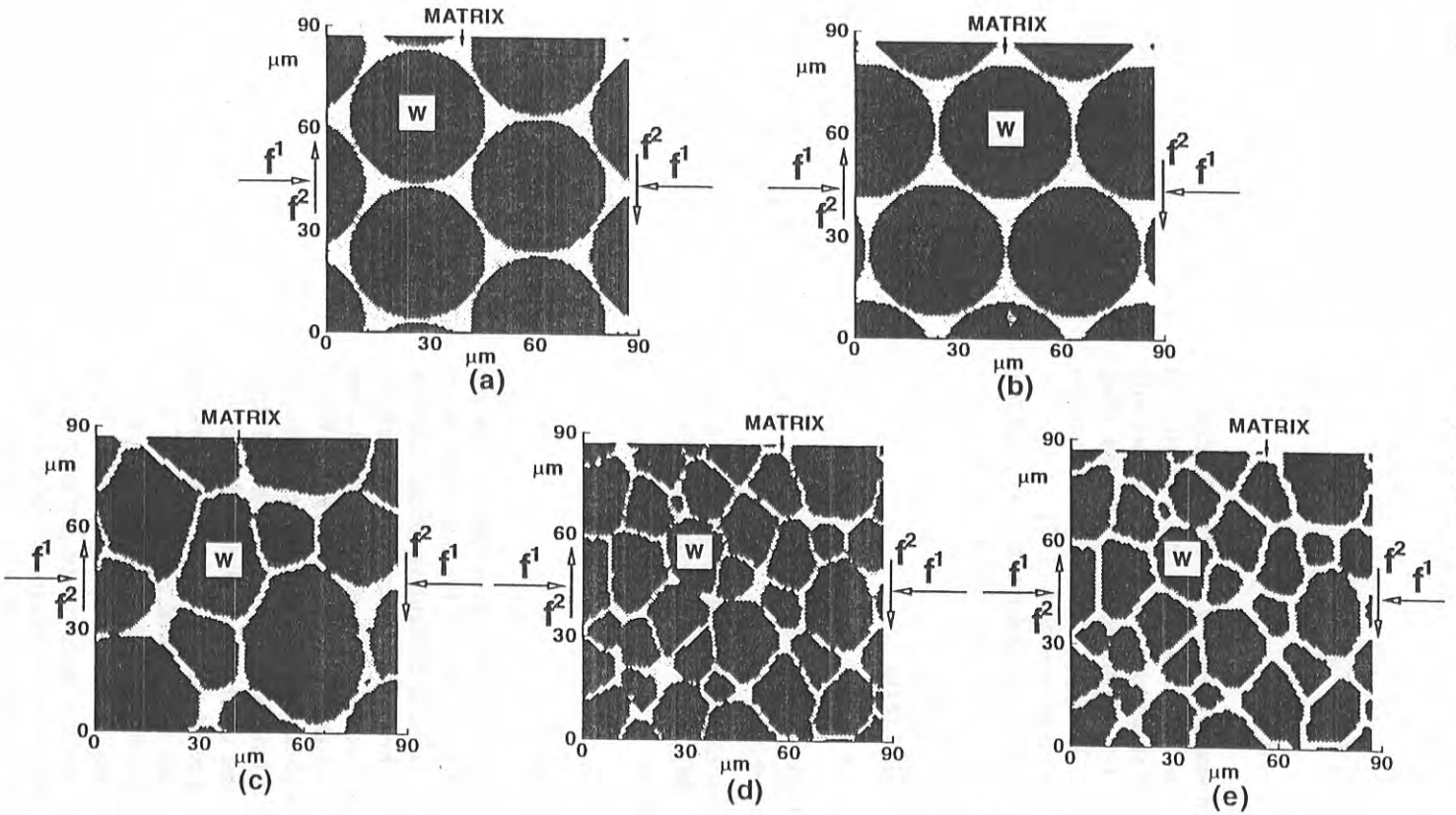

FIG. 6. Grain–matrix distributions used in the plane strain numerical analyses; (a) circular grains embedded in a soft matrix; (b) circular grains embedded in a soft matrix, obtained by rotating (a) by 90° counter-clockwise; (c) digitized microstructure from the micrograph of the actual alloy; (d) digitized microstructure with the grain size reduced by a factor of 1.75; (e) the same grain–matrix distribution as in (d) with the grain volume fraction reduced to 76.8%. Distributions (a)–(d) have the same grain volume fraction of 87.7%.

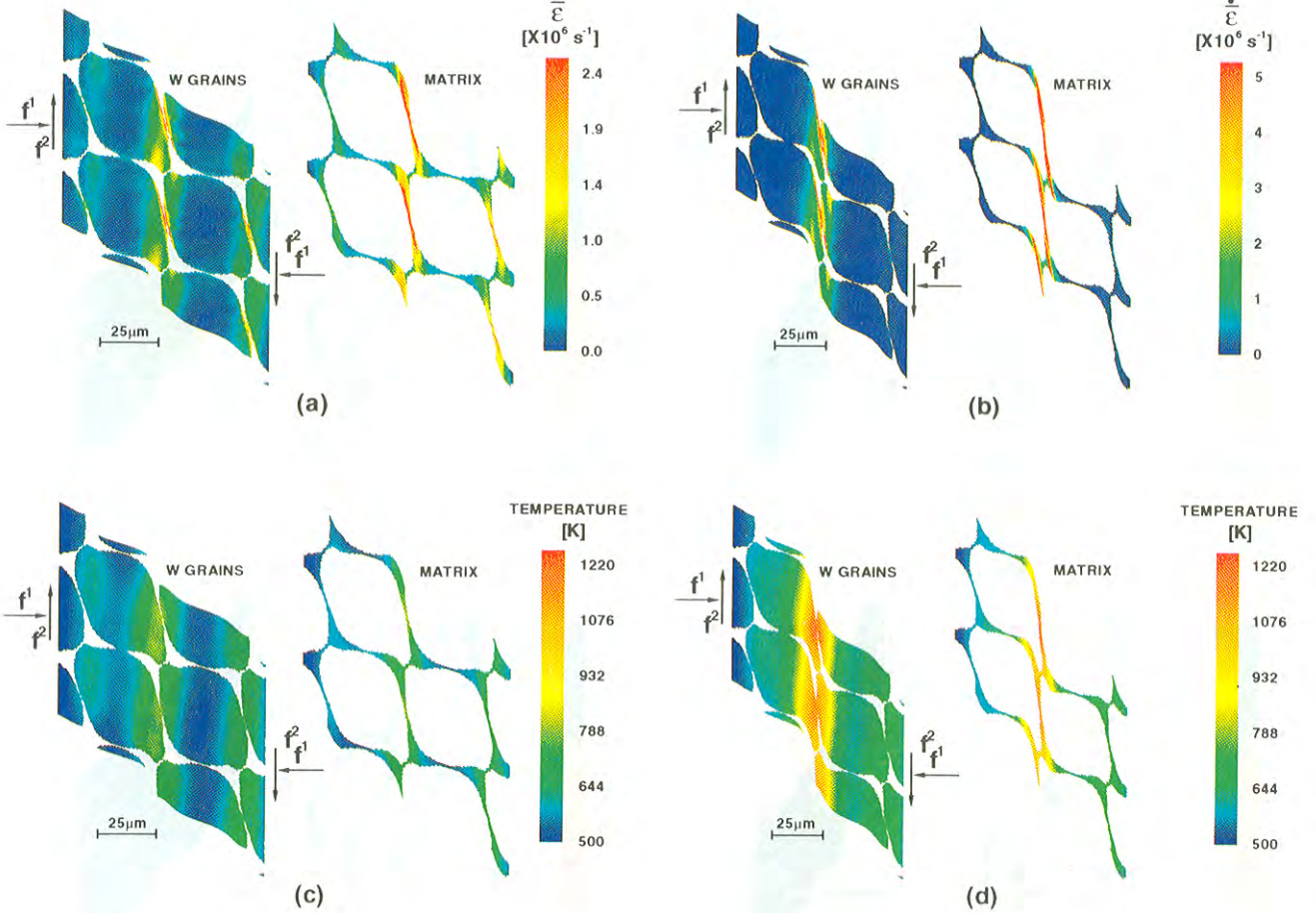

FIG. 8. Equivalent plastic strain rate $\dot{\bar{\varepsilon}}$ and temperature distributions for the grain–matrix distribution shown in Fig. 6(a). (a) $\dot{\bar{\varepsilon}}$ at 1.4 μs after impact; (b) $\dot{\bar{\varepsilon}}$ at 2 μs after impact; (c) temperature at 1.4 μs after impact; and (d) temperature at 2 μs after impact.

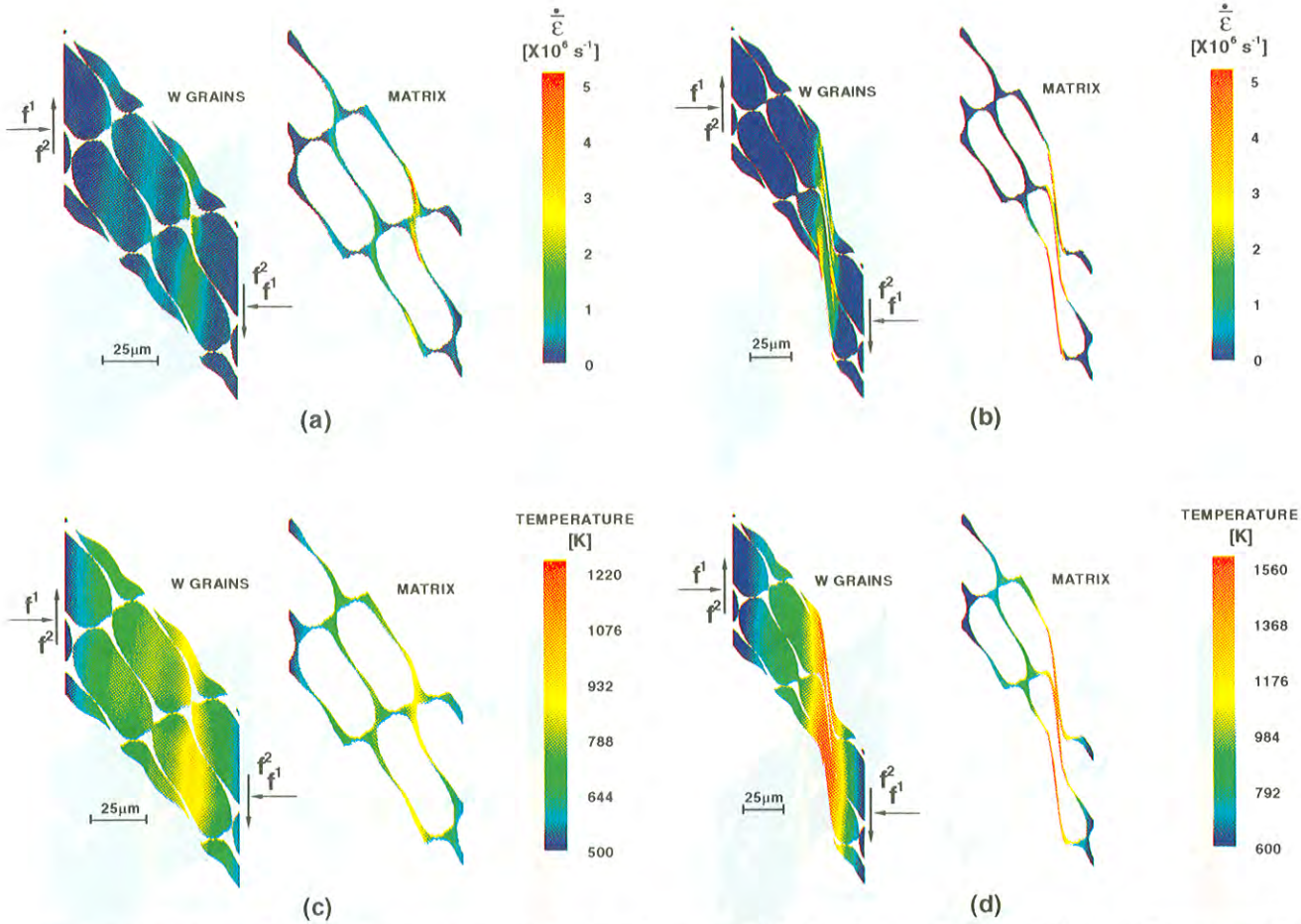

FIG. 10. Equivalent plastic strain rate $\dot{\bar{\varepsilon}}$ and temperature distributions for the grain–matrix distribution shown in Fig. 6(b). (a) $\dot{\bar{\varepsilon}}$ at 2 μs after impact; (b) $\dot{\bar{\varepsilon}}$ at 3 μs after impact; (c) temperature at 2 μs after impact; and (d) temperature at 3 μs after impact.

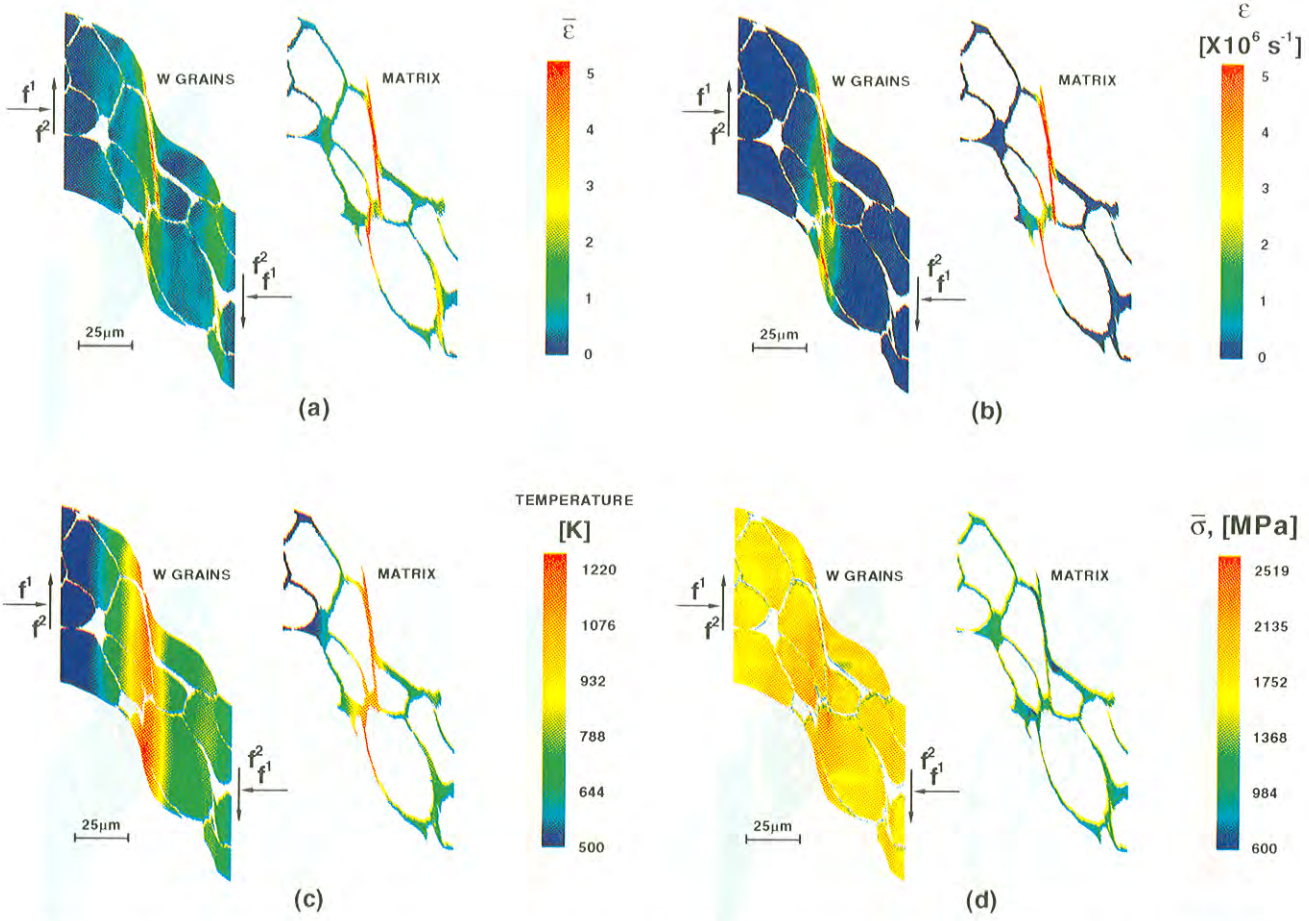

FIG. 12. Distributions of (a) $\dot{\bar{\varepsilon}}$; (b) $\bar{\varepsilon}$; (c) temperature; and (d) $\bar{\sigma}$ at 2 μs after impact for the digitized microstructure shown in Fig. 6(c).

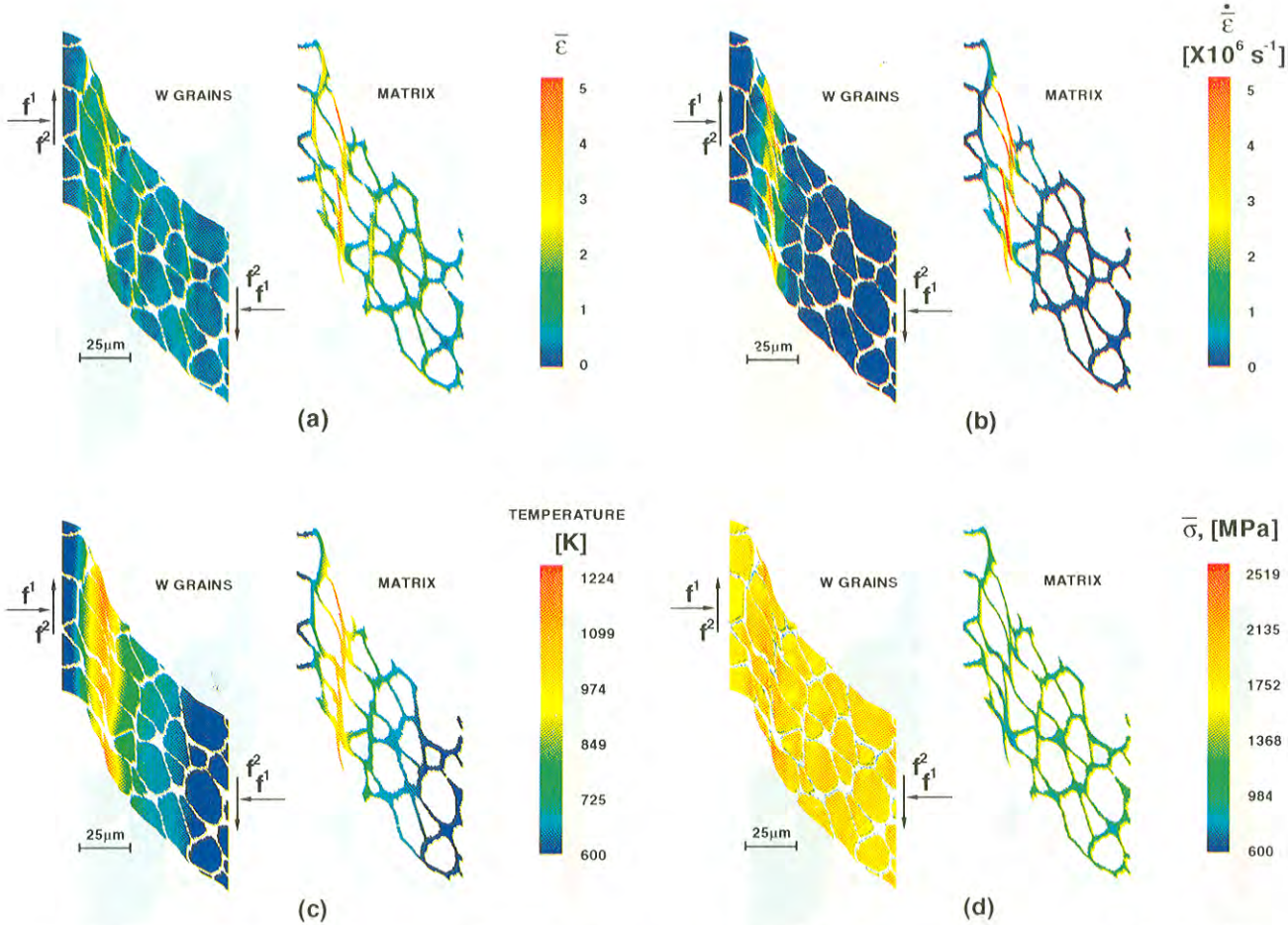

FIG. 15. Distributions of (a) $\dot{\bar{\varepsilon}}$; (b) $\bar{\varepsilon}$; (c) temperature; and (d) $\bar{\sigma}$ at 2 μs after impact for the grain–matrix distribution shown in Fig. 6(e).

The material parameters used for the tungsten grains and the matrix are listed in Table 1. The two constituent phases in the alloy possess quite different thermal and mechanical properties. The tungsten grains have high density, high flow strength, strong rate sensitivity, low strain hardening, high melting temperature and low specific heat. The matrix alloy has lower density, lower flow strength, weaker strain rate sensitivity, higher strain hardening, lower melting temperature and higher specific heat. The mechanical properties of the flyer and the anvil are also shown for reference.

In the numerical analyses, $\theta = 26.6°$, $V_0 = 202$ m s^{-1} and the specimen thickness $h = 87$ μm, as in the experiment that led to the shear band in Fig. 2(b). A square planar region, 87 μm $\times$ 87 μm, is used in the calculations. A coarse version of the finite element mesh (with 20×20 "crossed triangle" squares) is shown in Fig. 7. The mesh used in the simulations is an 80×80 uniform distribution of "crossed triangle" square elements. A finer mesh with 120×120 uniform square elements was used to investigate the dependence on mesh size; very little difference was found between the results obtained using the two element sizes.

Figures 8–11 present numerical results for the microstructures shown in Figs 6(a) and 6(b). First, the microstructure in Fig. 6(a) is considered. The distributions of equivalent plastic strain rate and temperature in the deformed configurations at 1.4 and 2.0 μs after impact are shown in Fig. 8. Figures 9(a)–(b) show the distributions of

TABLE 1. *Material parameters*

Tungsten grains (W)
$\dot{\varepsilon}_0 = 1.0 \times 10^{-4}\ \text{s}^{-1}$, $m = 50$, $\varepsilon_0 = 730$ MPa
$\dot{\varepsilon}_m = 8.0 \times 10^{8}\ \text{s}^{-1}$, $a = 21$
$\varepsilon_0 = 2.12 \times 10^{-5}$, $N = 0.05$
$\beta = 2.4$, $\kappa = 0.15$, $T_0 = 293$ K
$k = 160$ W (m·K)$^{-1}$, $c_p = 138$ J (kg·K)$^{-1}$,
$\rho = 19{,}300$ kg m^{-3}
$E = 4.00 \times 10^{5}$ MPa, $\nu = 0.29$
$\alpha = 5.3 \times 10^{-6}\ \text{K}^{-1}$
Matrix (Ni–W–Fe)
$\dot{\varepsilon}_0 = 1.0 \times 10^{-4}\ \text{s}^{-1}$, $m = 25$, $\sigma_0 = 150$ MPa
$\dot{\varepsilon}_m = 8.0 \times 10^{12}\ \text{s}^{-1}$, $a = 35$
$\varepsilon_0 = 5.88 \times 10^{-4}$, $N = 0.20$
$\beta = 2.4$, $\kappa = 0.20$, $T_0 = 293$ K
$k = 100$ W (m·K)$^{-1}$, $c_p = 382$ J (kg·K)$^{-1}$,
$\rho = 9200$ kg m^{-3}
$E = 2.55 \times 10^{5}$ MPa, $\nu = 0.29$
$\alpha = 1.5 \times 10^{-5}\ \text{K}^{-1}$
Flyer and anvil (tungsten carbide)
$\rho c_L = 106.89$ MPa m^{-1} s^{-1}, $\rho c_s = 59.997$ MPa m^{-1} s^{-1}
$k = 100$ W (m·K)$^{-1}$, $D^2 = 3.095 \times 10^{-5}$ m s^{-1}

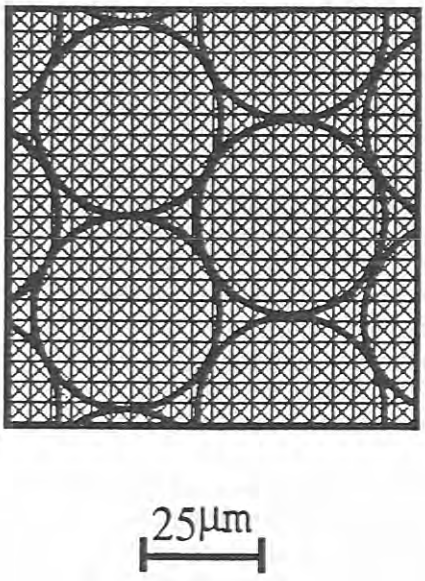

FIG. 7. A coarse version of the finite element mesh with 20×20 quadrilaterals; the actual mesh used in the simulations has 80×80 quadrilaterals.

accumulated equivalent plastic strain at 1.4 and 2.0 μs, respectively. The corresponding Mises equivalent stress distributions are shown in Figs 9(c)–(d). The contours show the development of a shear band at the center of the specimen. The formation of the band involves both the grains and the matrix. The deformed grains show tear-drop shapes, similar to those observed in the micrograph shown in Fig. 2(b).

Initially, the plastic strain rate is much higher in the matrix than in the tungsten grains because of the lower flow stress of the matrix. This imbalance is partially offset at intermediate times as the relatively high strain hardening rate of the matrix raises the flow stress in the matrix. Simultaneously, the heat generated in the matrix begins to soften the matrix and boundary layers of the neighboring grains, assisted by the high thermal conductivity of the tungsten. This process of progressive hardening of the matrix and progressive penetration of the thermal-softened layers of the tungsten grains continues until at $t = 1.4$ μs an emerging band of slightly higher plastic strain rate is discernible at the specimen center, Fig. 8(a), and the tails of the tear-drop shaped grains begin to appear. By 2.0 μs a shear band has developed, with the equivalent plastic strains inside the band reaching eight–nine and a peak temperature inside the band of 1219 K, which is approximately 70% of the melting temperature of the matrix (≈ 1750 K). At such large strains the mesh is very distorted and gradients within the band are not accurately resolved.

The distributions of strain, strain rate and temperature all give indications of the width of the shear band. Because of heat diffusion, the band of high temperatures is wider [Fig. 8(d)] than the band of high equivalent plastic strain rate [Fig. 8(b)]. Comparison with the shear band width observed in experiments is probably most

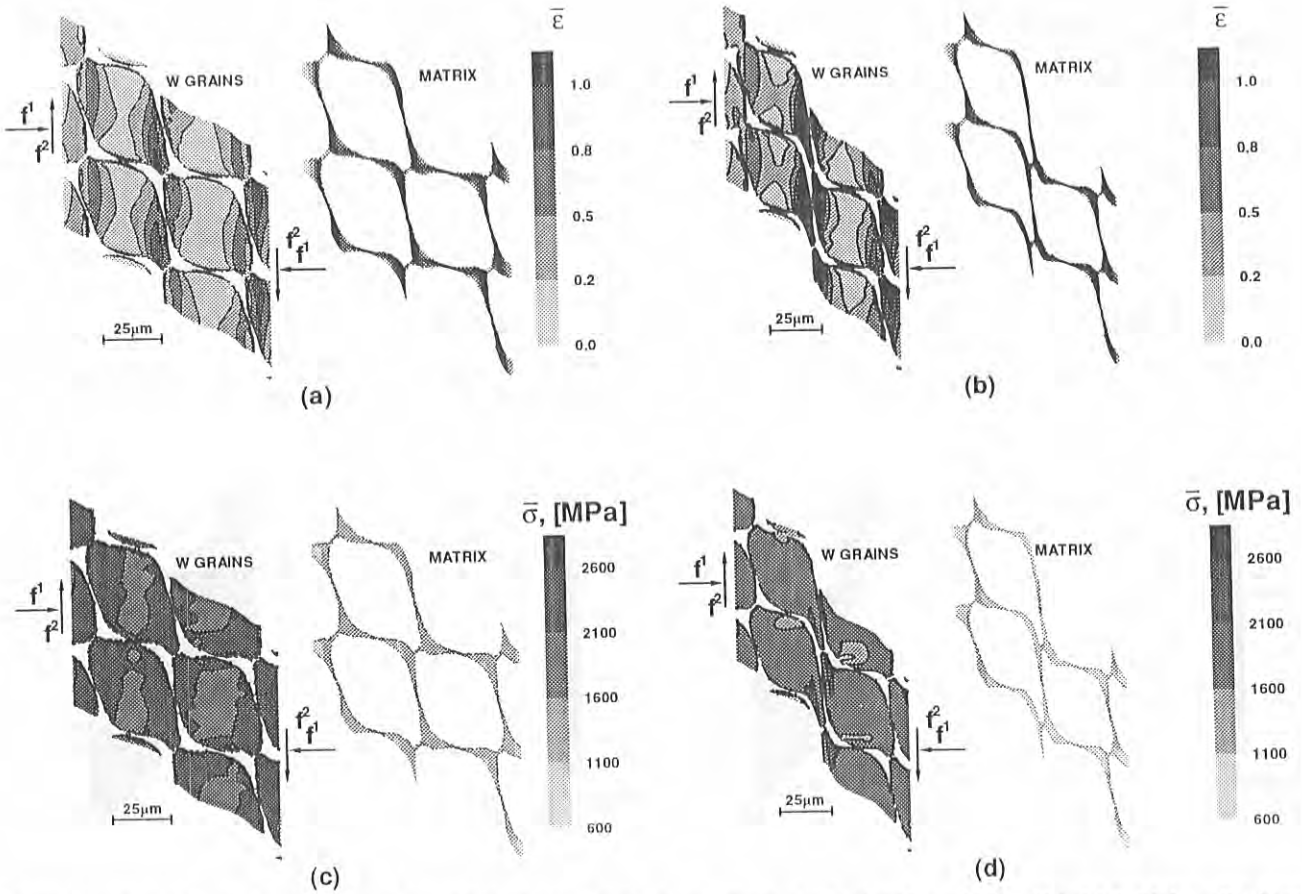

FIG. 9. Equivalent plastic strain $\bar{\varepsilon}$ and equivalent stress $\bar{\sigma}$ distributions for the grain–matrix distribution shown in Fig. 6(a). (a) $\bar{\varepsilon}$ at 1.4 μs after impact; (b) $\bar{\varepsilon}$ at 2 μs after impact; (c) $\bar{\sigma}$ at 1.4 μs after impact; and (d) $\bar{\sigma}$ at 2 μs after impact.

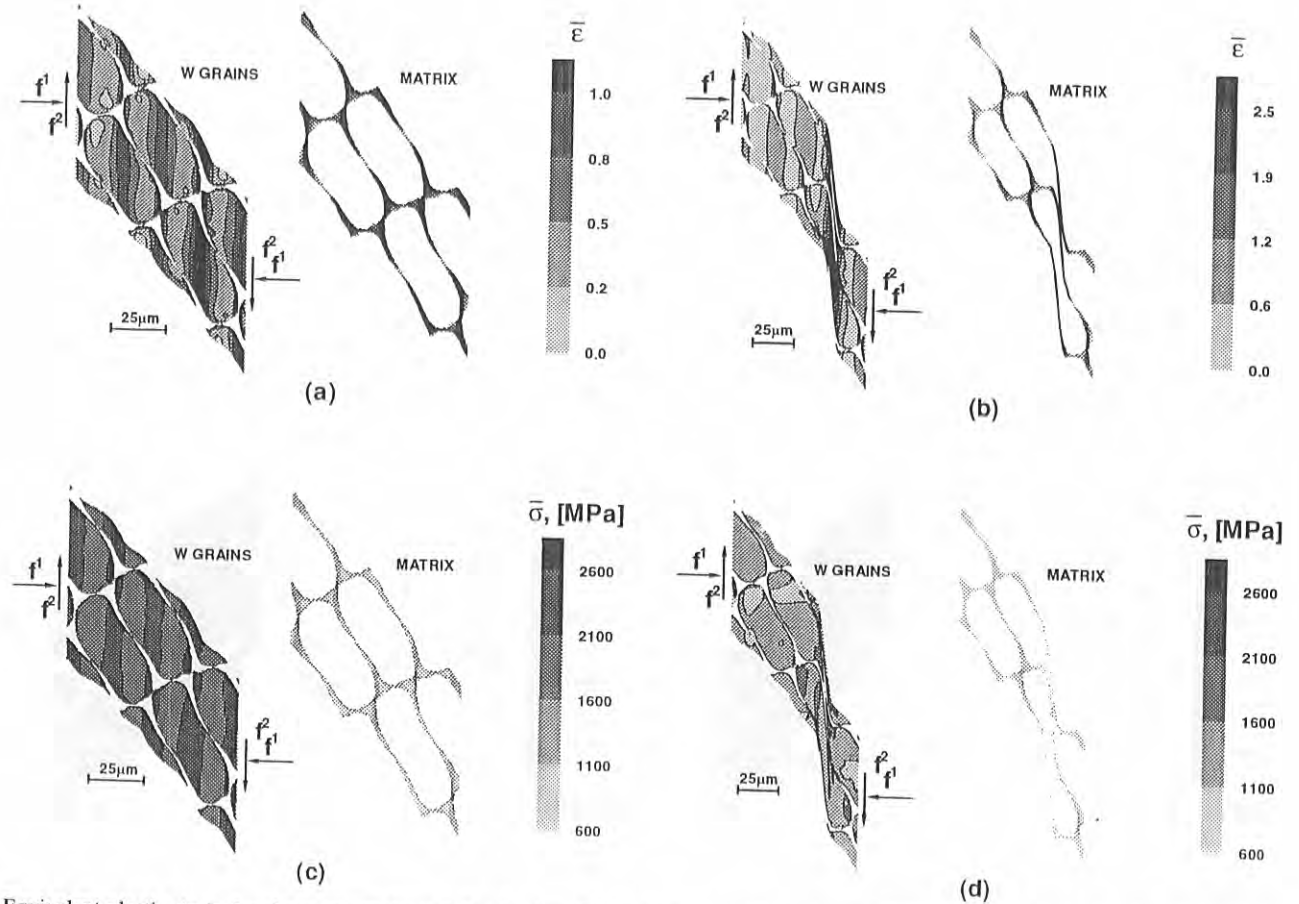

FIG. 11. Equivalent plastic strain $\bar{\varepsilon}$ and equivalent stress $\bar{\sigma}$ distributions for the grain–matrix distribution shown in Fig. 6(b). (a) $\bar{\varepsilon}$ at 2 μs after impact; (b) $\bar{\varepsilon}$ at 3 μs after impact; (c) $\bar{\sigma}$ at 2 μs after impact; and (d) $\bar{\sigma}$ at 3 μs after impact.

appropriately based on the distribution of equivalent plastic strain. In Fig. 9(b), the band of intense shear deformation has a width of approximately 10 μm, which is consistent with the band width in the micrograph in Fig. 2(b). As shown in Figs 9(c)–(d), the equivalent stress in the matrix is essentially uniform and is less than in the grains. The overall stress levels decrease due to thermal softening as the deformation progresses. Higher values of $\bar{\sigma}$ occur in the parts of the grains associated with the shear band. The hydrostatic pressure (not shown) is nearly the same in both the matrix and grains, and is approximately 9.7 GPa.

In contrast, shear band development is delayed for the interlocking distribution of the grains shown in Fig. 6(b). Figures 10(a)–(b) show the distributions of the equivalent plastic strain rate at 2.0 and 3.0 μs after impact, respectively. The corresponding temperature distributions are shown in Figs 10(c)–(d). The distributions of the equivalent plastic strain at 2.0 μs and 3.0 μs are shown, respectively, in Figs 11(a)–(b). A shear band has not formed at 2.0 μs due to the lack of a direct shear path through the soft matrix. The equivalent plastic strain rate distribution shown in Fig. 10(a) indicates an emerging band of higher strain rate. The band initiates from the matrix and runs through the grains that are in its path parallel to the shear direction. The shear band is fully developed at 3.0 μs, as seen in Figs 10(b), (d) and Figs 11(b), (d). The width of the band is still about 10 μm, as in Figs 8–9. The Mises equivalent stress distributions are shown in Figs 11(c)–(d). In Fig. 11(d), as in Fig. 9(d), $\bar{\sigma}$ attains somewhat higher values near the shear band than in other parts of the specimen.

The different responses calculated for shearing in the different orientations of Figs 6(a) and 6(b) indicate that the formation of shear bands in the two phase microstructure is dependent on the arrangement of the tungsten grains. Shear localization begins in the soft phase and propagates along a favorable path. Hard grains located in the paths of shear bands impede their development. In order to investigate the effects of grain arrangement, attention is now directed towards the microstructure obtained by digitizing a micrograph of the material that was actually used in the experiments.

The digitized microstructure shown in Fig. 6(c) is used for the analysis shown in Fig. 12, where the configuration after 2.0 μs is shown. A shear band has formed at the center of the specimen, the width of which is the same as for the cases shown in Figs 8–11. At 2.0 μs more intense shear deformation is obtained than for the cases of uniformly spaced circular grains. The peak equivalent plastic strain and temperature in the shear band are slightly higher than what is obtained in Figs 8 and 9. The average grain size in this digitized microstructure is 25–30 μm, significantly smaller than the grain diameter of 39.2 μm for the microstructures in Figs 6(a)–(b). The tails of the tear-drop shapes are similar to what is seen in Figs 8–11 for the circular grains. In addition, the overall shapes of the deformed grains more closely resemble those observed in the micrograph of Fig. 2(b).

The effect of decreasing the grain size is illustrated in Fig. 13, which shows the distributions of equivalent plastic strain rate and temperature at 2.0 and 3.0 μs after impact for the microstructure of Fig. 6(d). The distributions of equivalent plastic strain at 2.0 and 3.0 μs are shown in Figs 14(a)–(b). At 2.0 μs the deformation is relatively uniform and a shear band has not formed. The shear band becomes fully developed by 3.0 μs after impact [Figs 13(b)–(d)]. This is in contrast to Fig. 12 where

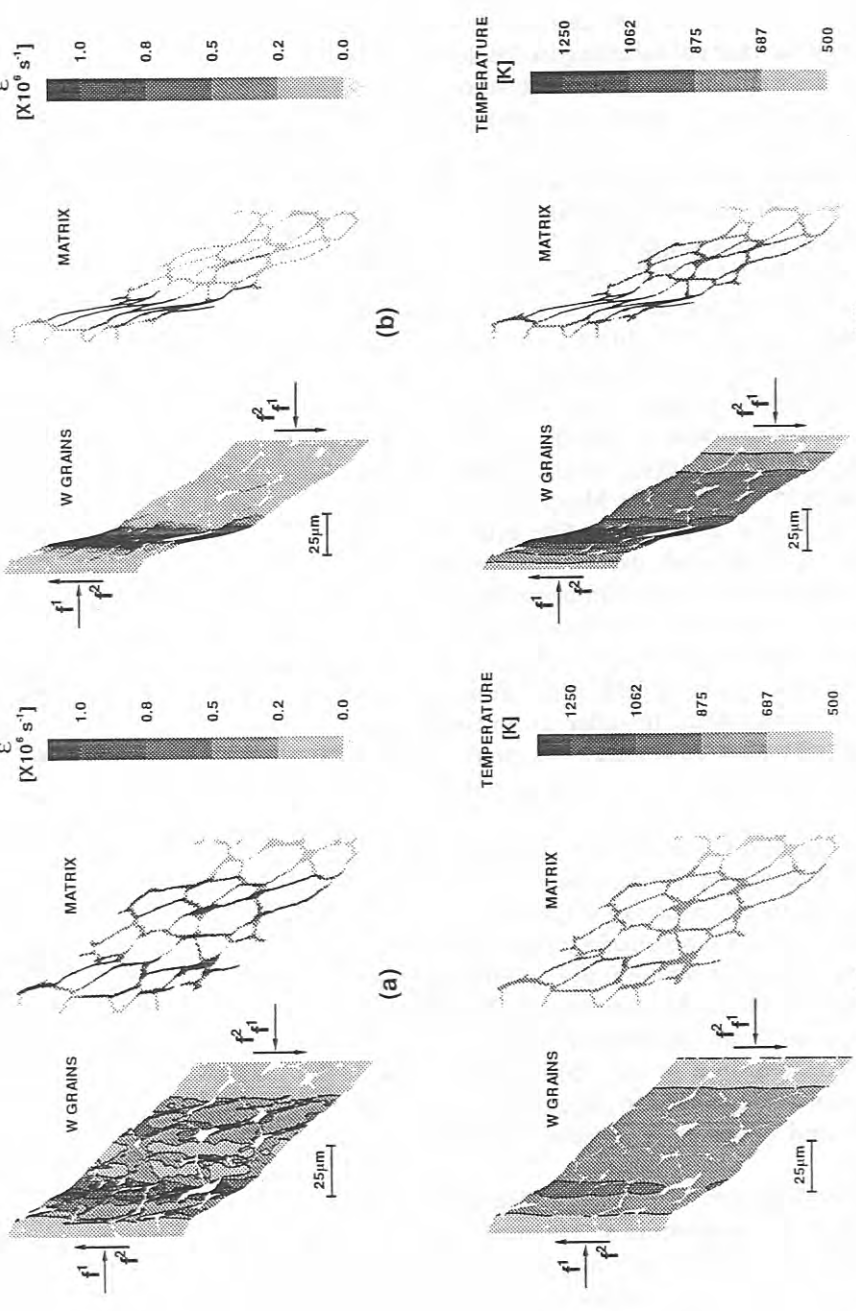

FIG. 13. Equivalent plastic strain rate $\dot{\bar{\varepsilon}}$ and temperature distributions for the grain–matrix distribution shown in Fig. 6(d). (a) $\dot{\bar{\varepsilon}}$ at 2 μs after impact; (b) $\dot{\bar{\varepsilon}}$ at 3 μs after impact; (c) temperature at 2 μs after impact; and (d) temperature at 3 μs after impact.

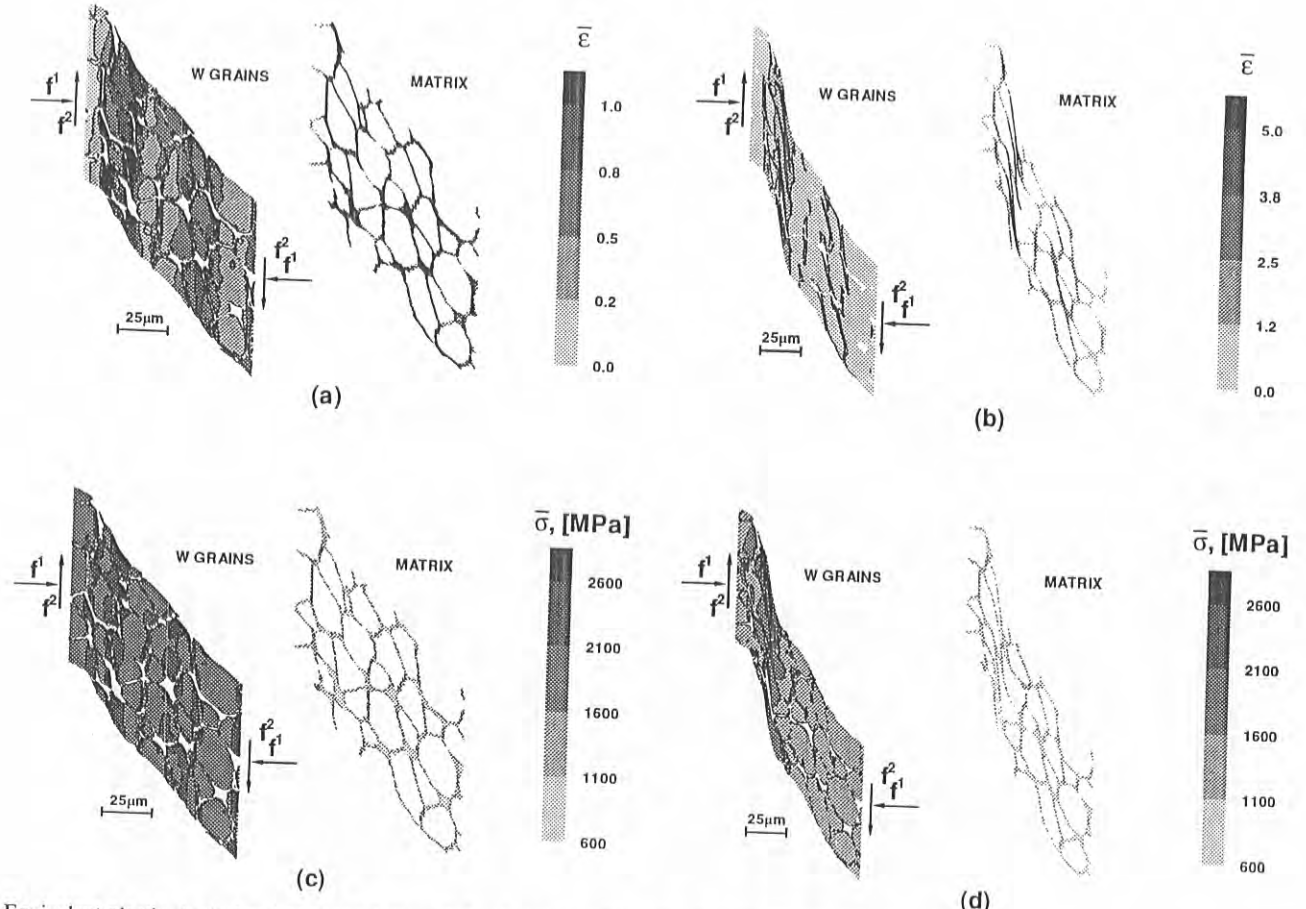

FIG. 14. Equivalent plastic strain $\bar{\varepsilon}$ and equivalent stress $\bar{\sigma}$ distributions for the grain–matrix distribution shown in Fig. 6(d). (a) $\bar{\varepsilon}$ at 2 μs after impact; (b) $\bar{\varepsilon}$ at 3 μs after impact; (c) $\bar{\sigma}$ at 2 μs after impact; and (d) $\bar{\sigma}$ at 3 μs after impact.

there is a fully developed shear band at 2.0 μs, which shows that shear band formation is delayed by the smaller grain size. This behavior is consistent with the linear perturbation analysis of CLIFTON (1980) in which it is shown that thermal conductivity tends to retard the formation of shear bands as the spatial frequency of the perturbations becomes large. Despite delaying the formation of a shear band, a smaller grain size does not change the width of the shear band. Figures 14(c)–(d) show that the Mises equivalent stress in the two phases is relatively uniform, consistent with the results for the other grain–matrix distributions.

Since the volume fractions of the phases can be changed by varying the composition of the alloy, the effect of phase volume fractions on localization behavior is of particular interest. Figure 15 shows the calculated fields at 2.0 μs after impact, for the microstructure of Fig. 6(e) in which the grain volume fraction is reduced to 76.8%. A shear band has developed, which is in contrast to the results shown in Figs 13–14, where the grain volume fraction is higher (87.7%) and a shear band is not fully developed until 3 μs after impact. Therefore, decreasing the grain volume fraction promotes shear band formation. Note that the width of the shear band is still about 10 μm. However, the band is located nearer to the flyer–specimen interface.

The effects of heat conduction are assessed by comparing the calculated results with heat conduction with those for the corresponding adiabatic case. Figure 16 shows distributions of equivalent plastic strain, equivalent plastic strain rate, temperature and equivalent stress at 0.6 μs after impact for an adiabatic calculation. All other parameters correspond to the case in Fig. 12 with the digitized microstructure in Fig. 6(c). Shear localization occurs much more rapidly when adiabatic conditions are assumed. Fully developed shear bands are found both at the center of the specimen and near the impact face [Figs 16(a)–(d)]. The catastrophic process of coupled increases in temperature and strain continues until the temperature inside the band reaches the melting point and the matrix loses all stress-carrying capacity. In the adiabatic simulation this occurs shortly after 0.6 μs. Heat conduction, of course, stabilizes the deformation and delays the formation of shear bands. Additionally, there is a significant effect on the shear band width. In the adiabatic case in Fig. 16, the shear band width is 1–2 μm, which corresponds to a width of one to two quadrilateral elements. In contrast, the shear band width of ≈ 10 μm in the analyses accounting for heat conduction is much greater than the element size.

One calculation was carried out for a case corresponding to transverse (grazing) impact, with θ in (3.20)–(3.22) equal to 90° and $V_0 = 202 \times \sin 26.6° = 90.45$ m s^{-1}. The results for the digitized microstructure of Fig. 6(c) are essentially the same as in Fig. 12, except that for the case in Fig. 12 a hydrostatic pressure of approximately 9.7 GPa is superposed. Thus, in the present context, where plastic flow is isochoric, independent of a superposed hydrostatic stress and no failure mechanism is operative, the impact angle only affects the magnitude of the hydrostatic stress.

6. DISCUSSION

Shear stress versus time curves and shear stress versus shear strain curves are shown in Fig. 17 for the five microstructures in Fig. 6. The nominal shear strain in Fig. 17(b)

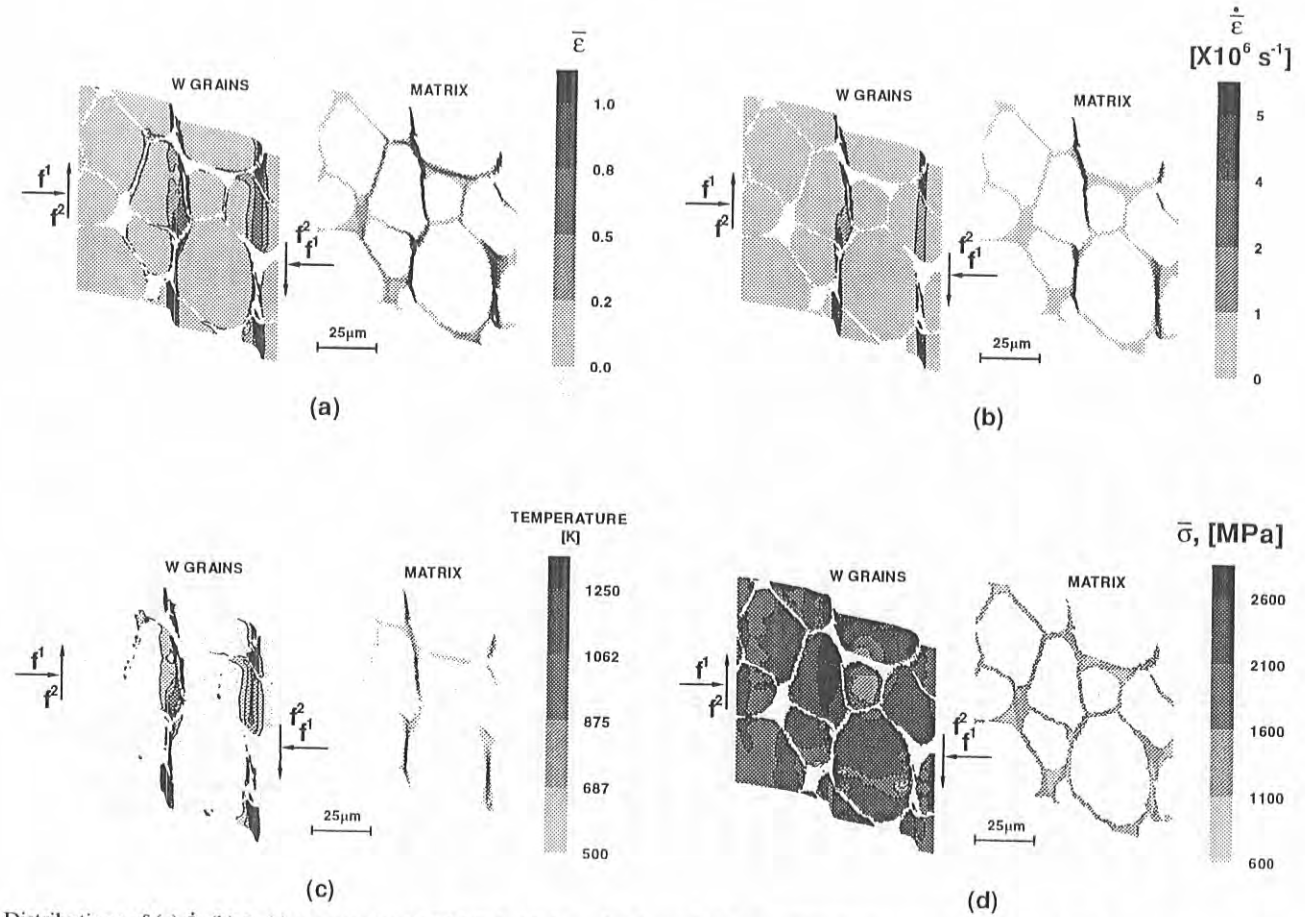

FIG. 16. Distributions of (a) $\dot{\bar{\varepsilon}}$; (b) $\bar{\varepsilon}$; (c) temperature; and (d) $\bar{\sigma}$ at 0.6 μs after impact for the digitized microstructure shown in Fig. 6(c) with adiabatic conditions assumed.

is the average shear strain across the specimen thickness or the difference between the transverse displacement components at the flyer–specimen interface and the specimen–anvil impact face divided by the initial specimen thickness h. The shear stress is the average value of the physical Cauchy stress component σ_{21} on the impact face. However, once significant plastic flow occurs, the shear stress is nearly uniform throughout the specimen in each of the calculations. The regime of principal interest in Fig. 17 is the regime, after approximately 0.1 μs, when the shear stress becomes nominally uniform through the specimen. The discrepancy between the calculated profiles and the experimental profile at earlier times is due to the inadequacy of the constitutive model at the high initial shearing rates, as mentioned previously, and experimental difficulties with measurements when the free surface particle velocity is changing sharply. The calculated stress–time profiles are based on instantaneous elastic response of the materials, resulting in high initial stresses followed by a rapid reduction in shear stress. The rate at which the shear stress decays is nominally proportional to the plastic shear strain rate, which could be higher if not limited by the limiting strain rate $\dot{\varepsilon}_m$. Several effects combine to make it extremely difficult for such an initial spike to be observed in experiments. Tilt between the impacting faces upon contact causes the wavefront to sweep across the finite spot size of the laser beam. Also, geometric dispersion due to the grain–matrix microstructure of tungsten carbide (the anvil material) causes the wavefront to spread as it propagates through the anvil. Nevertheless, after about 0.4 μs, there is very good agreement between the measured shear stress level and those computed for the digitized microstructure in Fig. 6(c) and the uniform grain distribution in Fig. 6(a). The digitized microstructure in Fig. 6(c) and the uniform grain distribution in Fig. 6(c) predict shear stress–shear strain curves very close to the experimental results during the initial stages of shear band development.

The experimental shear stress–time and shear stress–shear strain curves show a fairly sharp drop in stress near the end of the record, whereas the computed curves do not. This may be due to an inadequate characterization of the thermal softening behavior at temperatures approaching the melting temperature. Strength data is available only up to around 500 K (see Fig. 3). That data was smoothly extrapolated to the melting temperature. Another, possibly more realistic characterization, would

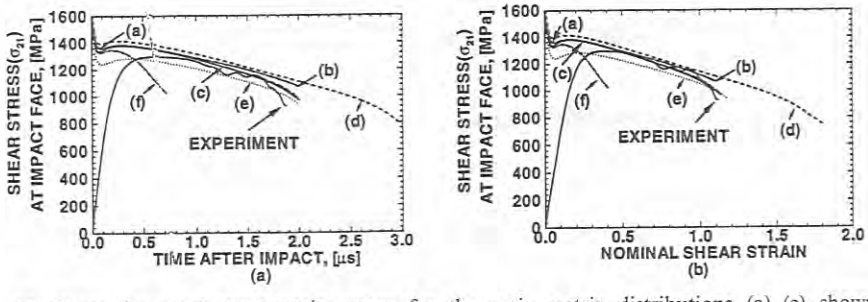

FIG. 17. Stress–time and stress–strain curves for the grain–matrix distributions (a)–(e) shown in Fig. 6; (f) corresponds to distribution (c) with adiabatic conditions assumed. (a) Stress–time curves; (b) stress–strain curves.

have the strength level off and then drop more abruptly near the melting temperature. The attainment of very high temperatures in the band would likely give a corresponding drop in the computed overall shear stress level. Another possible explanation for the lack of a sharp drop in the computed shear stresses in Fig. 17 is numerical. There may be mesh-induced stiffening stemming from the large mesh distortions that occur in the latter stages of the computations. In this regard, it is worth noting that the mesh is able to resolve the localized deformations that occur as well as it does because the preferred shear band direction is along element boundaries. The recovered specimens also show damage due to the nucleation and growth of voids and microcracks. However, such damage most likely occurs due to the tensile unloading wave that arrives at later times than those considered in the calculations.

The effect of grain volume fraction and distribution on the stress–strain response is shown in Fig. 17. The delay in shear band development for the interlocking arrangement of grains in Fig. 6(b) gives rise to a slower drop in shear stress. The smaller grain size of the distribution of Fig. 6(d) strengthens the WHA by causing the deformation to be more uniform and by delaying the development of localized deformation. The lower grain volume fraction in Fig. 6(e) reduces the stress level of the alloy and expedites the formation of shear bands. The effect of heat conduction on the shear-stress is seen by comparing curves (c) and (f) in Fig. 17. The conduction of heat greatly stabilizes the deformation by reducing thermal softening.

The development of localization in rate dependent, thermally softening solids is an evolutionary process and there is interest in exploring the possibility of obtaining relatively simple criteria for various stages in the development of localization. One approach has been to use an energy criterion to identify stages in the localization process, in particular variations in the kinetic energy (SHAWKI *et al.*, 1992). Figure 18 shows the evolution of the kinetic energy for each of the simulations based on the microstructures in Fig. 6. The difference between the curves in Fig. 18 comes, at least partly, from the dependence of the velocity distribution on the location of the shear band. For the heterogeneous microstructures analysed here, unlike for the homogeneous solids analysed in ZBIB and JUBRAN (1992), there is no clear correlation between changes in kinetic energy and the development of localization. However, even though intense shear localization takes place, no abrupt stress drop occurs in the calculations.

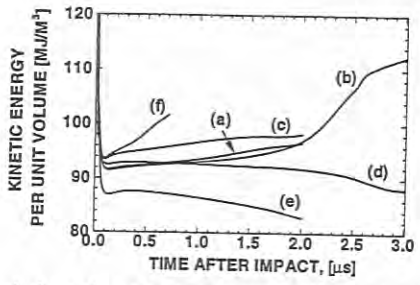

FIG. 18. Kinetic energy evolutions for the grain–matrix distributions (a)–(e) shown in Fig. 6; (f) corresponds to distribution (c) with adiabatic conditions assumed.

ZHOU (1993) showed that shear bands were not formed when pure tungsten and the matrix (a nickel–iron–tungsten alloy with similar composition and processing was used as a model material) were tested separately under pressure–shear impact and dynamic torsion. This behavior is in contrast to the susceptibility to shear banding demonstrated by the composite tungsten heavy alloy. Calculations were carried out for homogeneous materials with the properties of the tungsten grains and the matrix alloy. Since the materials are homogeneous, the deformations are independent of ξ^2 and an 80×1 quadrilateral mesh was used in these calculations.

Figure 19 shows the distributions of the equivalent plastic strain [Fig. 19(a)], equivalent plastic strain rate [Fig. 19(b)], and temperature [Fig. 19(c)] across the specimen thickness, at 2 μs after impact, for pure tungsten and for the matrix. For comparison purposes, the corresponding results are also shown for the WHA simulation based on the digitized microstructure of Fig. 6(c). The curves for the digitized WHA microstructure represent averages over the ξ^2 direction. Neither the pure tungsten nor the matrix shows the formation of a shear band, but the WHA composite does. Calculated shear stress versus time profiles for the one-dimensional calculations of Fig. 19 are shown in Fig. 20(a). The corresponding shear stress versus nominal shear strain curves are shown in Fig. 20(b). Pure tungsten has much higher

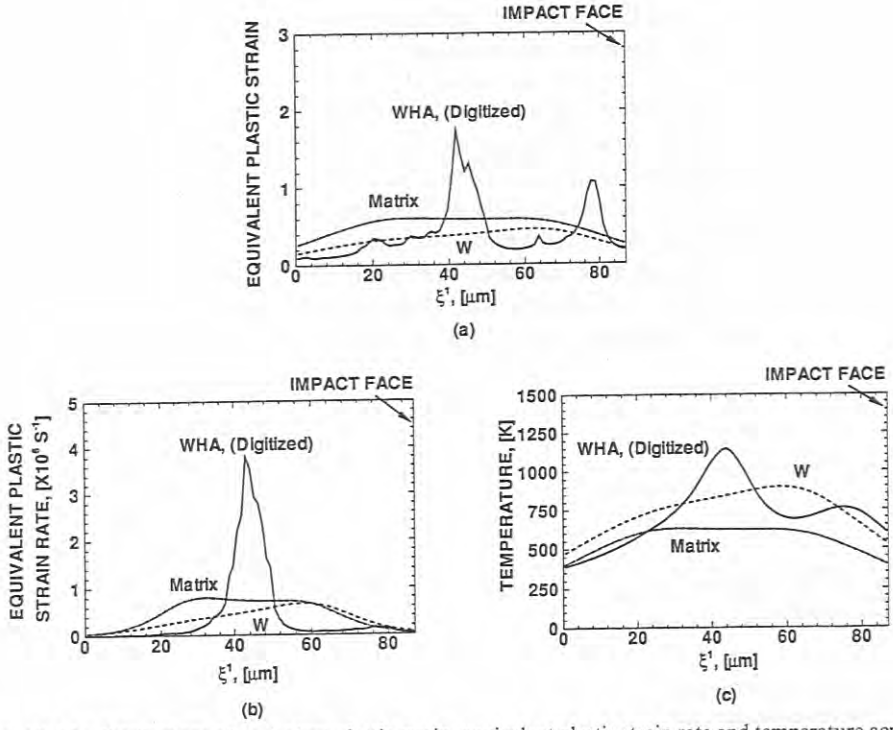

FIG. 19. The distributions of equivalent plastic strain, equivalent plastic strain rate and temperature across the specimen thickness for W, matrix and WHA, under the same impact conditions, at $t = 2$ μs. (a) Equivalent plastic strain; (b) equivalent plastic strain rate; (c) temperature.

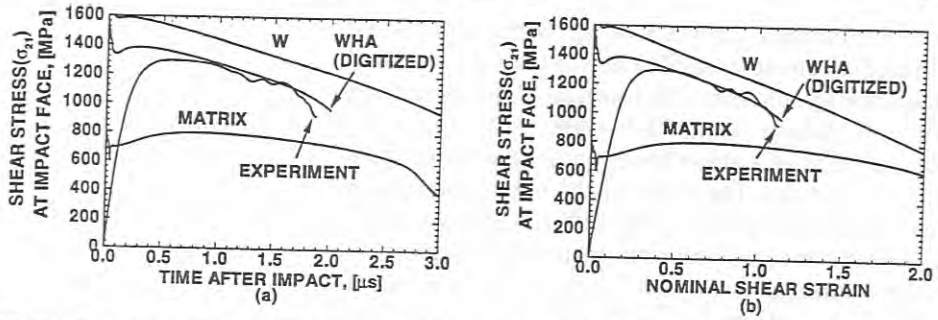

FIG. 20. Stress–time and stress–strain curves for W, matrix and WHA under the same impact conditions. The experimental curve is also shown. (a) Stress–time curves; (b) stress–strain curves.

flow stress than the matrix. The high flow stress in tungsten causes high rates of heat generation, but, because of the high melting temperature of tungsten, thermal softening is not sufficiently strong to cause localization. The matrix does eventually exhibit localization, but at rather late times ($\approx 2.75\ \mu$s) and at very large strains. Thus, in the composite, the inhomogeneities arising from the presence of the tungsten grains provide perturbations for initiating localization in the matrix at much earlier times. However, in order for a shear band to form, the harder tungsten grains must undergo large deformations. The progressive thermo-mechanical coupling between the phases causes both of them to be involved in the formation of the shear band. Depending on grain morphology and volume fraction the band can, in principle, occur either earlier or later than when localization would occur in the matrix alone; however, for the experiments and computations conducted in this investigation, localization always occurred earlier in the composite.

A shear band width of about 10 μm has been obtained for all cases considered here (see Figs 8–15), except for the adiabatic case (Fig. 16). This width agrees well with what is observed experimentally [Fig. 2(b)]. The computations have shown that the shear band width is insensitive to changes in grain arrangement, grain shape, grain size and grain volume fraction. On the other hand, a strong dependence on the thermal conductivity has been found. The dependence of the width on heat conductivity and strain rate was analysed by MERZER (1982). DODD and BAI (1985) derived the following approximate relationship

$$w = \sqrt{\frac{k\Delta T}{\chi \bar{\sigma}\dot{\bar{\varepsilon}}}}, \tag{5.1}$$

between the half width, w, of the shear band and the temperature difference ΔT between the inside and the outside of the band. In (5.1) the denominator is the fraction of plastic dissipation rate that is converted to heat. From Fig. 14, for $\Delta T \approx 400$ K, $\bar{\sigma} \approx 1800$ MPa, and $\dot{\bar{\varepsilon}} \approx 2.0 \times 10^6\ \mathrm{s}^{-1}$, one obtains $2w = 7.7\ \mu$m.

The characteristic length set by heat conduction is $L^* = 2\sqrt{D^2 t^*}$ where t^* is a time scale of the process and $D^2 = k/\rho c_p$ is the thermal diffusivity. Two time scales need to be considered: (a) the local characteristic time associated with the formation of a

shear band; this characteristic time determines the width of the band; and (2) the duration of the experiment over which the conduction of heat into the flyer and anvil takes place; this characteristic time strongly influences the location of the shear band relative to the interfaces. For the present study $D^2 = 4.91 \times 10^{-5}$ m^2 s^{-1}, $\bar{t} = 1/\dot{\gamma} = 2.89 \times 10^{-7}$ s for the development of a shear band, with $\dot{\gamma}$ the shear strain rate inside it. Therefore, $\bar{L} = 2\sqrt{D^2 \bar{t}} \approx 7.5$ μm. The width of the band generated in the computations [e.g. the mid-height width of the band in Fig. (19b)] is approximately 8 μm. Thus, the width of the shear band correlates well with the characteristic length set by heat conduction. The duration of the experiment is $\hat{t} = 2.0 \times 10^{-6}$ s. The length scale for heat conduction through the boundaries is $\hat{L} = 2\sqrt{D^2 \hat{t}} \approx 19.8$ μm. This length is consistent with Figs 8(d), 10(d), 12(d), 13(d) and 15(d) where heat conduction significantly influences the temperature distribution over approximately 1/5–1/4 of the specimen thickness near each of the two boundaries. This influence of heat conduction is clearly demonstrated by the difference between the results of Fig. 12 (with heat conduction) and Fig. 16 (without heat conduction). Heat conduction into the anvil effectively prevented one of the shear bands in Fig. 16 (the one that is approximately 10 μm away from the impact face) from forming in Fig. 12. This indicates that heat conduction directly influences the formation of shear bands by preventing the localization from occurring near the impact face where the shearing rates are high initially.

Indeed, heat conduction plays an important role in dynamic shear band development in the pressure–shear plate impact experiment. It contributes to sustaining the stress carrying capacity and to stabilizing the deformation. Furthermore, it sets the length scale for the width of the shear band (note that when heat conduction is accounted for the shear band width is clearly not set by the mesh) and influences the location of the region where localized deformation takes place.

The analyses here have been carried out in a two-dimensional plane–strain context. The assumption of plane strain deformations is appropriate for the pressure–shear plate impact experiments over the time interval considered. The main limitation of the two-dimensional framework is associated with modelling the material microstructure in terms of cylindrical grains. A full three-dimensional analysis would require substantially greater computational resources. Also, the tungsten grains have been modelled as elastically isotropic and in the plastic range, as isotropically hardening Mises solids. Any effect of elastic anisotropy, or of plastic flow occurring on discrete slip systems has been neglected. Nevertheless, key features of the observed phenomenology of shear localization in tungsten heavy alloys under pressure–shear plate impact are reproduced by the computations. Furthermore, the computational framework permits the effects of variations of microstructure on the localization behavior to be explored.

ACKNOWLEDGEMENT

The work of M.Z. and R.J.C. was supported by the Army Research Office through grant No. DAAL03-91-G-0025, and the work of A.N. was supported by the Brown University MRG on "Micro-Mechanics of Failure-Resistant Materials" funded by the U.S. National Science

Foundation. The computations were carried out on a Cray YMP computer at the San Diego Supercomputer Center.

References

ANDREWS, E. W., BOWER, A. F. and DUFFY, J. (1992) Shear band formation in a tungsten heavy alloy. *Proc. Symp. Shear Bands and Viscoplastic Theories, The 29th Annual Technical Meeting of the Soc. for Engng Sci.*, 14–16 Sep., La Jolla, CA.

BAI, Y. L. (1981) A criterion for thermo-plastic shear instability. *Proc. Int. Conf. on Metallurgical Effects of High-strain-rates Deformation and Fabrication*, Albuquerque, NM, pp. 277–283. Plenum, NY.

BAI, Y. L. (1982) Thermo-plastic instability in simple shear. *J. Mech. Phys. Solids* **30**(4), 195–207.

BATRA, R. C. and KIM, C. H. (1992) Analysis of shear banding in twelve materials. *Int. J. Plasticity* **8**, 425–452.

BELYTSCHKO, T., CHIAPETTA, R. L. and BARTEL, H. D. (1976) Efficient large scale non-linear transient analysis by finite elements. *Int. J. Numer. Meth. Engng* **10**, 579–596.

BOSE, A., SIMS, D. and GERMAN, R. M. (1988) Test temperature and strain rate effects on the properties of a tungsten heavy alloy. *Metall. Trans. A* **19A**, 487–494.

CLIFTON, R. J. (1980) Adiabatic shear banding. *Material Response to Ultra-high Loading Rates*, NMAB-356, Chapter 8. National Materials Advisory Board (NRC), Washington, D.C.

CLIFTON, R. J. and KLOPP, R. W. (1985) Pressure-shear plate impact testing. *Metals Handbook*, Vol. 8, 9th edition, pp. 230–239. Amer. Soc. Metals, Metals Park.

DODD, B. and BAI, Y. (1985) Width of adiabatic shear bands. *Mater. Sci. Technol.* **1**, 38–40.

DUFFY, J. and CHI, Y. C. (1992) On the measurement of local strain and temperature during the formation of adiabatic shear bands. *Mater. Sci. Engng* **A157**, 195–210.

KRIEG, R. D. and KEY, S. W. (1973) Transient shell response by numerical time integration. *Int. J. Numer. Meth. Engng* **7**, 273–286.

LEE, E. H. (1969) Elastic–plastic deformation at finite strains. *J. Appl. Mech.* **36**, 1–6.

LEMONDS, J. and NEEDLEMAN, A. (1986) Finite element analyses of shear localization in rate and temperature dependent solids. *Mech. Mater.* **5**, 339–361.

MERZER, A. M. (1982) Modelling of adiabatic shear band development from small imperfections. *J. Mech. Phys. Solids* **30**(5), 323–338.

MOLINARI, A. and CLIFTON, R. J. (1987). Analytical characterization of shear localization in thermoviscoplastic materials. *Trans. ASME, J. Appl. Mech.* **54**, 806–812.

NEEDLEMAN, A. (1989). Dynamic shear band development in plane strain. *J. Appl. Mech.* **56**, 1–9.

NEEDLEMAN, A. and TVERGAARD, V. (1991) An analysis of dynamic, ductile crack growth in a double edge cracked specimen. *Int. J. Fract.* **49**, 41–67.

NEEDLEMAN, A. and TVERGAARD, V. (1992) Analyses of plastic flow localization in metals. *Appl. Mech. Rev.* **45**, S3–S18.

O'DONNELL, R. G. and WOODWARD, R. L. (1990) The composition and temperature dependence of the mechanical properties of tungsten alloys. *Metall. Trans. A.* **21A**, 744–748.

PEIRCE, D., SHIH, C. F. and NEEDLEMAN, A. (1984) A tangent modulus method for rate dependent solids.. *Comp. Struct.* **18**, 875–887.

POVIRK, G. L., NUTT, S. R. and NEEDLEMAN, A. (1993) Continuum modelling of residual stress in metal-matrix composites. *Residual Stresses in Composites: Measurement, Modelling and Effect on Thermo-Mechanical Properties*, to be published.

RECHT, R. F. (1964) Catastrophic thermoplastic shear. *J. Appl. Mech.* **86**, 189–193.

SHAWKI, T. G. and CLIFTON, R. J. (1989) Shear band formation in thermal viscoplastic materials. *Mech. Mater.* **8**, 13–43.

SHAWKI, T. G., SHERIF, R. A. and CHERUKURI, H. P. (1992) Characterization of severe localization in dynamic viscoplasticity. *Appl. Mech. Rev.* **45,** S149–S153.

TAYLOR, G. I. and QUINNEY, H. (1934) The latent energy remaining in a metal after cold working. *Proc. R. Soc.* **A143,** 307–326.

WRIGHT, T. W. and WALTER, J. W. (1987) On stress collapse in adiabatic shear bands. *J. Mech. Phys. Solids* **35**(6), 701–720.

ZBIB, H. M. and JUBRAN, J. S. (1992) Dynamic shear banding: a three-dimensional analysis. *Int. J. Plasticity* **8,** 619–641.

ZHOU, M. (1993) Dynamic Shear Strain Localization in a Tungsten Heavy Alloy and Ductile Rupture in a Spheroidized 1045 Steel. Brown University Ph.D. Thesis, Providence, RI.

ZHOU, M., CLIFTON, R. J. and NEEDLEMAN, A. (1992) Shear band formation in a W–Ni–Fe alloy under plate impact. In *Tungsten and Tungsten Alloys*—1992, pp. 343–356. Metal Powder Industries Federation, Princeton, NJ.